

5-2010

A LYAPUNOV BASED APPROACH TO ENERGY MAXIMIZATION IN RENEWABLE ENERGY TECHNOLOGIES

Erhun Iyasere

Clemson University, oiyaser80@gmail.com

Follow this and additional works at: https://tigerprints.clemson.edu/all_dissertations



Part of the [Electrical and Computer Engineering Commons](#)

Recommended Citation

Iyasere, Erhun, "A LYAPUNOV BASED APPROACH TO ENERGY MAXIMIZATION IN RENEWABLE ENERGY TECHNOLOGIES" (2010). *All Dissertations*. 526.

https://tigerprints.clemson.edu/all_dissertations/526

This Dissertation is brought to you for free and open access by the Dissertations at TigerPrints. It has been accepted for inclusion in All Dissertations by an authorized administrator of TigerPrints. For more information, please contact kokeefe@clemson.edu.

A LYAPUNOV BASED APPROACH TO ENERGY MAXIMIZATION IN
RENEWABLE ENERGY TECHNOLOGIES

A Dissertation
Presented to
the Graduate School of
Clemson University

In Partial Fulfillment
of the Requirements for the Degree
Doctor of Philosophy
Electrical Engineering

by
Erhun Iyasere
May 2010

Accepted by:
Dr. Darren Dawson, Committee Chair
Dr. John Wagner
Dr. Timothy Burg
Dr. Ian Walker

ABSTRACT

This dissertation describes the design and implementation of Lyapunov-based control strategies for the maximization of the power captured by renewable energy harnessing technologies such as (i) a variable speed, variable pitch wind turbine, (ii) a variable speed wind turbine coupled to a doubly fed induction generator, and (iii) a solar power generating system charging a constant voltage battery.

First, a torque control strategy is presented to maximize wind energy captured in variable speed, variable pitch wind turbines at low to medium wind speeds. The proposed strategy applies control torque to the wind turbine pitch and rotor subsystems to simultaneously control the blade pitch and tip speed ratio, via the rotor angular speed, to an optimum point at which the capture efficiency is maximum. The control method allows for aerodynamic rotor power maximization without exact knowledge of the wind turbine model. A series of numerical results show that the wind turbine can be controlled to achieve maximum energy capture.

Next, a control strategy is proposed to maximize the wind energy captured in a variable speed wind turbine, with an internal induction generator, at low to medium wind speeds. The proposed strategy controls the tip speed ratio, via the rotor angular speed, to an optimum point at which the efficiency constant (or power coefficient) is maximal for a particular blade pitch angle and wind speed by using the generator rotor voltage as a control input. This control method allows for aerodynamic rotor power maximization without exact wind turbine model knowledge. Representative numerical results

demonstrate that the wind turbine can be controlled to achieve near maximum energy capture.

Finally, a power system consisting of a photovoltaic (PV) array panel, dc-to-dc switching converter, charging a battery is considered wherein the environmental conditions are time-varying. A backstepping PWM controller is developed to maximize the power of the solar generating system. The controller tracks a desired array voltage, designed online using an incremental conductance extremum-seeking algorithm, by varying the duty cycle of the switching converter. The stability of the control algorithm is demonstrated by means of Lyapunov analysis. Representative numerical results demonstrate that the grid power system can be controlled to track the maximum power point of the photovoltaic array panel in varying atmospheric conditions. Additionally, the performance of the proposed strategy is compared to the typical maximum power point tracking (MPPT) method of perturb and observe (P&O), where the converter dynamics are ignored, and is shown to yield better results.

DEDICATION

To my family.

ACKNOWLEDGMENTS

I thank Dr. Timothy Burg and Dr. Ian Walker, my committee members for their technical guidance. I express deep gratitude to my advisor Dr. Darren Dawson for being the yard-stick by which I strive daily to measure myself against. I thank my Co-advisor Dr. John Wagner for his support and guidance throughout my graduate study at Clemson.

I thank Jesse Black for the friendship, support and hard work. I thank Enver Tatlicioglu for the selfless work, guidance and interest in my professional well-being.

I thank all my colleagues who helped me during the course of my graduate work: Nitendra Nath, Ninad Pradhan, Mohammed Salah, Ryan Lusso, Thomas Mitchell, Apoorva Kapadia, David Braganza, and Thomas Cash.

I would also like to thank all my friends in Clemson whose support helped me considerably.

TABLE OF CONTENTS

	Page
TITLE PAGE	i
ABSTRACT	ii
DEDICATION	iv
ACKNOWLEDGMENTS	v
LIST OF TABLES	viii
LIST OF FIGURES	ix
CHAPTER	
I. INTRODUCTION	1
Nonlinear Robust Control to Maximize Energy Capture in a Variable Speed Wind Turbine.....	2
Nonlinear Robust Control to Maximize Energy Capture in a Variable Speed Wind Turbine Using an Induction Generator	4
Backstepping PWM Control for Maximum Power Tracking in Photovoltaic Array Systems	8
Organization of Dissertation	12
References.....	12
II. NONLINEAR ROBUST CONTROL TO MAXIMIZE ENERGY CAPTURE IN A VARIABLE SPEED WIND TURBINE	18
Problem Statement	18
Dynamic Model Development.....	19
Error System Development.....	21
Stability Analysis	23
Estimation of System Nonlinearities	26
Trajectory Generator.....	30
Simulation Results	31
References.....	35

Table of Contents (Continued)

	Page
<p>III. NONLINEAR ROBUST CONTROL TO MAXIMIZE ENERGY CAPTURE IN A VARIABLE SPEED WIND TURBINE USING AN INDUCTION GENERATOR.....</p>	36
Problem Statement.....	36
Nomenclature.....	37
System Model.....	38
Controller Design.....	42
Nonlinear Observer Design.....	51
Trajectory Generator.....	55
Simulation Results.....	57
References.....	65
<p>IV. BACKSTEPPING PWM CONTROL FOR MAXIMUM POWER TRACKING IN PHOTOVOLTAIC ARRAY SYSTEMS.....</p>	66
Problem Statement.....	66
Photovoltaic Array System Dynamics.....	66
Controller Design.....	68
Stability Analysis.....	70
Generating the Desired Array Voltage Online.....	72
Simulation Results.....	73
References.....	79
<p>APPENDICES.....</p>	83
A: Proof of Lemma 2.1.....	84
B: Simulation Parameters for Chapter 2.....	85
C: Generating the Stator Flux Online.....	86
D: Auxiliary Signal Definitions.....	88
E: Design of Bounding Terms.....	92
F: Proof of Lemma 3.1.....	93
G: Simulation Parameters for Chapter 3.....	94

LIST OF TABLES

Table		Page
4.1	List of simulation parameters and corresponding values.....	74
B.1	Simulation parameters and values	85
G.1	Simulation parameters and values	94

LIST OF FIGURES

Figure	Page
1.1 Current-voltage characteristics of a PV array	9
1.2 Power-voltage characteristics of a PV array	10
2.1 Desired rotor speed $\omega_d(t)$ and actual rotor speed $\omega(t)$	33
2.2 Desired blade pitch $\beta_d(t)$ and actual blade pitch $\beta(t)$	33
2.3 Power coefficient function C_p versus tip-speed ratio λ , and blade pitch angle β , for the simulated wind turbine.....	34
2.4 Maximum rotor power coefficient $C_p(t)$ resulting from the numerical optimization algorithm	34
2.5 Simulated control torque for (a) drive train subsystem, $\tau_\omega(t)$ and pitch subsystem $\tau_\beta(t)$	35
3.1 Rotor speed tracking error $e(t)$	58
3.2 Stator flux tracking error $\eta_{s_1}(t)$	59
3.3 Stator flux tracking error $\eta_{s_2}(t)$	59
3.4 Rotor flux tracking error $\eta_{r_1}(t)$	60
3.5 Rotor flux tracking error $\eta_{r_2}(t)$	60
3.6 Voltage control input $V_{r_1}(t)$	61
3.7 Voltage control input $V_{r_2}(t)$	61

List of Figures (Continued)

Figure	Page
3.8 Power efficiency curve of the simulated wind turbine	62
3.9 Rotor power coefficient $C_p(t)$ resulting from optimization algorithm.....	62
3.10 Rotor Speed $\omega(t)$	63
3.11 Copper losses $P_{loss}(t)$	63
3.12 Desired Stator flux $\Psi_{s_1}^d(t)$	64
3.13 Nonlinearity observation error $\tilde{f}(t)$	64
4.1 The system structure of the photovoltaic array system.....	67
4.2 Temperature and solar radiation conditions present in the simulation.....	75
4.3 Array voltage tracking error $e(t)$	76
4.4 Duty ratio $D(t)$	76
4.5 Desired array voltage $V_d(t)$	77
4.6 Actual and maximum PV array power.....	77
4.7 Power obtained when converter dynamics are ignored	78
4.8 Integral square error performance measure	78

CHAPTER ONE

INTRODUCTION

There is a considerable need to find an alternative to conventional means of power generation for logistical, environmental and geo-political reasons. Renewable energy technologies, which are defined as technologies that capture power from naturally replenishing energy sources, present such an alternative. Example sources include sunlight, geothermal, wind, and water (tide and hydroelectric). However, renewable energy accounts for about 18% of global energy consumption combined. In order to make a bigger contribution to global power demand, it is imperative that the said technologies be as efficient as possible in capturing power from the energy sources. This increase in the capacity factor of renewable energy capture technology will make renewable technologies a more viable alternative to conventional power generation systems. This dissertation is presented in three sections, each of which addresses a different control problem associated with power maximization of a renewable energy technology and the ensuing Lyapunov-based control approach. This dissertation is divided in three parts: power capture efficiency maximization of a variable speed, variable pitch wind turbine, power capture efficiency maximization of a fixed pitch, variable speed wind turbine coupled to a doubly fed induction generator and power maximization of a solar generating system charging a battery.

Nonlinear Robust Control to Maximize Energy Capture in a Variable Speed Wind Turbine

Wind energy has evolved into an attractive energy source for electric utilities, even though it is currently responsible for only two percent of the global electrical power output. The structure of wind turbines, as well as the fact that the wind energy rate is uncontrollable, compounds the problem of regulating the power capture of the wind turbine. This problem has been alleviated by the construction of variable speed wind turbines; which are designed to regulate the power captured over a range of wind speeds. The efficiency of power regulation, is however dependent on the selected control method.

Wind turbine control methods include classical techniques [1]-[3], which utilize a linearized wind turbine system model and a single measured wind turbine output for control. In [2], a PID controller was designed that compensated for wind speed fluctuations by changing the pitch angle to keep the rotor speed constant. The controller was improved by selecting gain values based on minimization of rotor speed error and the actuator duty cycle. Another common control method is full state feedback control [4]-[7], which is sensitive to errors in modeling and measurements. Liebst [4] used individual blade pitch linear quadratic Gaussian (LQG) optimal control to reduce the loads on a wind turbine due to environmental factors such as shear and gravity. The dynamics of the wind turbine blade flap, lag and pitch are modeled. Knudsen et al. [5] compared PI and H_∞ controllers for regulating the pitch of a 400kW wind turbine. The H_∞ controller accounts better for turbine model uncertainties as well as error in measuring the wind speed, thus reducing pitch activity. Disturbance accommodating control can account for measurement disturbances by augmenting a state-estimator based controller to recreate

disturbance states using an assumed waveform model. These new states reduce disturbance effects. Wright and Balas [8] described the design of a state space control algorithm for the regulation of the rotor speed of a two bladed wind turbine in full-load operation using a simple five degree-of-freedom linear model. The authors demonstrated that the pole placement technique can stabilize the turbine model while state estimators reduce the number of required measurements. The effects of wind speed fluctuations were reduced by using disturbance accommodating control.

Fuzzy logic control [9]-[11] and neural networks [12] have been investigated to reduce the uncertainties faced by classical control methods. Prats et al. [10] presented a fuzzy logic application for enhanced energy capture in a variable speed, variable pitch wind turbine. A dynamic model was developed using torque and blade pitch fuzzy control and produced better results than linear control. Zhang et al. [11] compared PID and fuzzy logic control in the control of the rotation of the wind wheel and reverse moment of the generator in a variable speed wind turbine and concluded that fuzzy logic control produce a smoother output with less susceptibility to disturbances. Adaptive control schemes [13]-[16] have been developed to eliminate some of the problems faced in wind turbine control, such as unknown and time varying model parameters in the wind turbine model. Song et al. [14] used a model reference adaptive control scheme to force a wind turbine with a known power efficiency function, to track a desired rotor speed that maximizes the energy captured by controlling the excitation winding voltage of the generator. Johnson et al. [15] developed an adaptive control algorithm for controlling the generator torque on a fixed pitch variable speed wind turbine. This approach maximized

the energy capture in low to medium wind speeds without knowledge of the optimal tip speed ratio.

In this study, a control strategy is developed to regulate the blade pitch angle and rotor speed of a variable speed wind turbine system. The control objective is to maximize the energy captured by the wind turbine in low to medium wind speeds by tracking a desired pitch angle and rotor speed, in the presence of structurally uncertain wind turbine system nonlinearities. Additionally, the maximization of the energy captured is achieved without the knowledge of the relationship that governs the power capture efficiency of the wind turbine. Instead, an optimization algorithm is developed to seek the unknown optimal blade pitch angle and rotor speed that maximize the energy captured (via the aerodynamic rotor power) while ensuring that the resulting desired trajectories are sufficiently differentiable. The disadvantage of not explicitly knowing the optimal pitch angle and rotor speed *a priori* is countered by the fact that the optimal rotor speed, and likewise, the optimal pitch angle, will change as the wind speed changes, which can be accounted for by the optimization algorithm. A robust controller is designed and proven to yield a globally uniformly ultimately bounded (GUUB) stable closed loop system through Lyapunov-based analysis.

Nonlinear Robust Control to Maximize Energy Capture in a Variable Speed Wind Turbine Using an Induction Generator

As previously stated, the efficiency of power regulation in wind turbines, is dependent on the selected control method. In this study, an in-depth investigation is conducted by considering the dynamics of the wind turbine internal generator in addition

to the mechanical dynamics. The standard region 2 (power capture maximization mode) control scheme used for variable speed wind turbines, ($\tau = k\omega^2$, where τ is the control torque, ω is the rotor angular speed and k is a control gain), has some disadvantages that can result in unsatisfactory power capture. First, the control gain k is difficult to determine due to the dependence on exact model knowledge (maximum power efficiency constant and optimal tip speed ratio). Secondly, the standard value of k might not provide the maximum energy capture under real world turbulent conditions. Johnson and Fingersh [15] showed via simulation/numerical results that smaller values of k than the standard can result in increased power capture. They proposed a new control scheme, specifically, an adaptive control scheme that allowed for maximum power capture in the presence of parameter uncertainty. Similar adaptive control techniques for wind turbine control were developed in [14] and [16].

Other wind turbine control methods such as classical control techniques [1], [4], [5], [7], robust control [17], and fuzzy logic control [9], [11] have been utilized to regulate rotor speed, regulate pitch angle and to enhance energy capture. Iyasere et al. [17] proposed a robust control strategy to control the blade pitch angle and rotor speed in a variable speed, variable pitch wind turbine in order to maximize the energy capture, without the knowledge of the optimal tip speed ratio and in the presence of model structural uncertainties.

An area of particular importance is the control of the internal generators used in wind turbines. The most commonly used generator is the induction generator; the types of which include cage, wound rotor and doubly fed induction generator (DFIG). The

dynamic modeling [18]-[22] and control [23]-[30] of induction machines have been extensively researched. Thiringer and Luomi [18] examined the validity of various dynamic models of induction machines to include the fifth-order Park model and other reduced order models by predicting the low frequency dynamic response of a 15 kW induction machine and comparing results to actual measurements. They concluded that the Park model accurately predicts rotor speed, electrical torque, active power, reactive power and stator current responses to perturbations in the shaft torque, supply frequency and voltage magnitude. In power system analysis, a third order model was determined to be the right fit for accuracy and simplicity. Tapia et al. [19] developed the mathematical model of a grid connected wind driven DFIG and presented a comparison of the simulation results to real machine performance results. They also developed a stator-flux-oriented vector control based technique to control the generator power factor. Mullane and O'Malley [20] examined the inertial response of a squirrel cage and a doubly fed induction wind turbine generator using fifth-order induction generator models. They discovered that a DFIG utilizing field-oriented control is strongly influenced by rotor current controller bandwidth. Hu and Dawson [23] presented an adaptive partial state feedback position tracking controller for the full-order nonlinear dynamic model for an induction motor. The controller compensates for uncertainty in rotor resistance and mechanical system parameters while yielding asymptotic rotor position tracking. Datta and Ranganathan [24] developed a simple position-sensorless strategy for rotor-side field-oriented control of a wound rotor induction machine. The algorithm is based on axis transformation with reduced dependence on machine parameters compared to other

methods. Pena et al. [25] described a vector control scheme for the supply-side voltage source-converter of a DFIG for independent control of active and reactive power. This strategy was embedded into an optimal tracking controller in order to maximize energy capture in a wind energy application. Two tracking schemes were developed; speed mode and current mode.

In this study, a control strategy is developed to regulate the rotor speed of a small variable speed wind turbine system with an induction generator. The control objective is to maximize the energy captured by the wind turbine for low to medium air speeds by tracking a desired rotor speed in the presence of system nonlinearities and structural uncertainty. Additionally, the maximization of the energy captured is achieved without the knowledge of the relationship that governs the power capture efficiency of the wind turbine. Instead, an optimization algorithm is developed to seek the unknown optimal rotor speed that maximizes the energy captured (via the aerodynamic rotor power), at a particular blade pitch angle and wind speed, while ensuring that the resulting trajectory is sufficiently differentiable. The problem of not explicitly knowing the rotor speed *a priori* is countered by the fact that the optimal rotor speed will change as the wind speed changes which may be accommodated for by choosing the right optimization algorithm. A robust controller is designed and proven to yield a globally uniformly ultimately bounded (GUUB) stable closed loop system through Lyapunov-based analysis.

Backstepping PWM Control for Maximum Power Tracking in Photovoltaic Array Systems

Solar energy is one of the more attractive sources of energy today owing to the rising costs of traditional energy sources, an increase in environmentalism and the inexhaustibility of the source of energy. The primary device for harnessing solar energy is the solar cell, which uses the photovoltaic effect to transform sunlight into electricity via a semiconductor device. Conditions such as cell parameters and atmospheric conditions (temperature and solar irradiation) affect the instantaneous energy generated by a PV array as demonstrated by the current-voltage ($i_{pv} - v_{pv}$) characteristic shown in Fig. 1.1 which can be mathematically described as follows [31]:

$$i_{pv} = n_p I_{ph} - n_p I_{rs} \left(e^{\frac{q v_{pv}}{n_s A K T}} - 1 \right) \quad (1.1)$$

where $i_{pv}(t) \in \mathbb{R}$ is the PV array output current; $v_{pv}(t) \in \mathbb{R}$ is the PV array output voltage; n_s is the number of cells connected in series; n_p represents the number of parallel modules; q is the charge of an electron; K is the Boltzmann's constant; A is the p - n junction ideality factor; and T is the cell temperature in Kelvin (K). The reverse saturation current, $I_{rs} \in \mathbb{R}$, and the photocurrent, $I_{ph} \in \mathbb{R}$, can be expressed as:

$$I_{rs} = I_{or} \left(\frac{T}{T_r} \right)^3 e^{\frac{q E_{go}}{K T} \left(\frac{1}{T_r} - \frac{1}{T} \right)} \quad (1.2)$$

$$I_{ph} = \left(I_{sc} + K_l (T - T_r) \right) \frac{\lambda}{100} \quad (1.3)$$

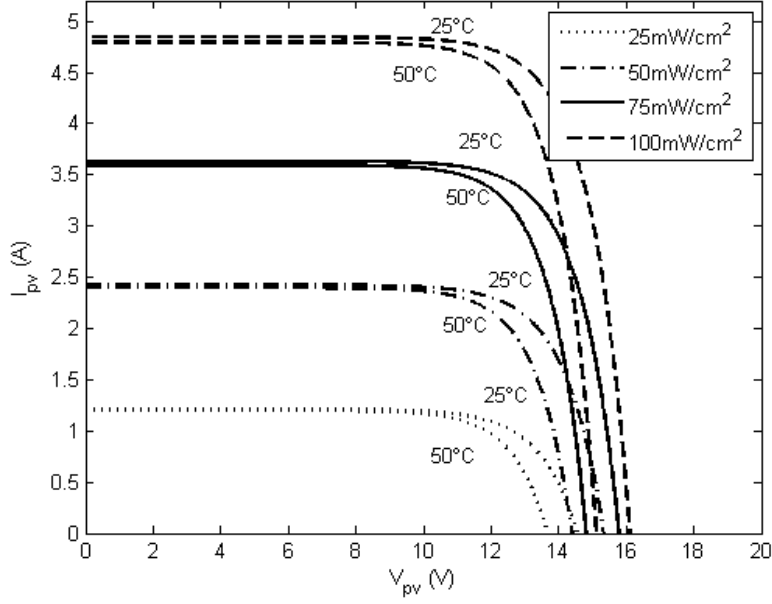


Figure 1.1: Current-voltage characteristics of a PV array

where I_{or} is the reverse saturation current at the reference temperature, T_r ; E_{go} is the band gap energy of the semiconductor; I_{sc} is the short-circuit cell current at the reference temperature and radiation; K_l is the short-circuit current temperature coefficient; and λ is the solar radiation in mW / cm^2 . Thus, the PV array output power, $P_{pv}(t)$, can be calculated as:

$$P_{pv} = i_{pv} v_{pv} = n_p I_{ph} v_{pv} - n_p I_{rs} v_{pv} \left(e^{\frac{q v_{pv}}{n_s A K T}} - 1 \right) \quad (1.4)$$

It can be concluded that exists a maximum power point (MPP) that varies with solar radiation and cell temperature as shown in Fig. 1.2. To this end, several control

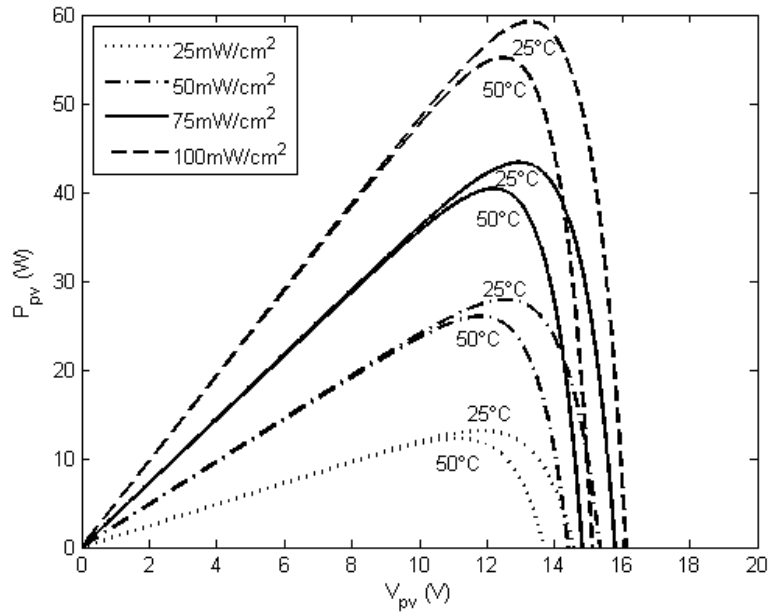


Figure 1.2: Power-voltage characteristics of a PV array

approaches has been developed to optimize the power output when atmospheric conditions are varying. An area of particular importance is the development of online extremum-seeking algorithms which are generally classified into incremental conductance (IncCond) [32]-[34] and “perturb and observe” (P&O) methods [35], [36]. Hussein et al. [32] developed a maximum power tracking (MPT) technique that is efficient in cases of rapidly changing atmospheric conditions. They showed that the maximum power operating point can be tracked accurately by measuring the solar array current and voltage, comparing the incremental and instantaneous conductances of the PV and changing the array voltage accordingly. Leyva et al. [35] demonstrated the global stability of an MPPT algorithm using Lyapunov analysis and applied it to a PV system based on the “perturb and observe” method. Control techniques used to directly control

photovoltaic characteristics include classical control [37]-[39], fuzzy logic control [31], robust control [36], [40], variable structure [41], [42], and artificial neural networks [43]-[45]. Lian et al. [31] regulate the output power of a solar power generating system using the Takegi-Sugeno fuzzy method which includes using virtual desired variables (VDVs). Kasa et al. [36] presents a robust control method for maximum power point (MPP) tracking in a photovoltaic system where the circuit parameters are uncertain. The MPP is tracked by varying the duty ratio of the switching device in order to control the array voltage. Valenciaga et al. [41] designed a variable structure controller to regulate the output power of a standalone hybrid generation system consisting of a PV array, wind turbine, a storage battery bank and a variable monophasic load.

Aside from maximizing the output power, another common application for photovoltaic arrays is load matching [36], [46], [47]. Saied et al. [46] maximized the output mechanical energy of a DC motor, driving a mechanical load, connected to a PV array via a dc-dc converter with varying atmospheric conditions. Yadaiah et al. [36] developed a controller algorithm to match a solar cell array to a mechanical load using artificial neural networks.

In this study, a control strategy is developed to maximize the power of a solar generating system while including the dynamics of the DC-DC converter that assumed absent in some papers. The control objective is to determine the maximum power operating point (MPOP) by tracking a desired array voltage which can be achieved by modulating the pulse width of the switch control signal (increasing or decreasing the duty ratio of the switching converter). The desired array voltage is designed online using a

filtered incremental conductance MPP tracking algorithm. The proposed strategy ensures that the MPOP is determined and the tracking errors are globally asymptotically regulated. The stability of the control algorithm is verified by Lyapunov analysis.

Organization of Dissertation

The dissertation is organized as follows. The development of a robust control strategy to maximize the power efficiency capture of a variable speed, variable pitch wind turbine is presented in Chapter 2. A robust control strategy to maximize the power capture efficiency of a fixed pitch, variable speed wind turbine coupled to a doubly fed induction generator is proposed in Chapter 3. A backstepping PWM controller is developed to maximize the power of a solar generating system with a constant battery load in Chapter 4. A summary of the presented works will be presented in Chapter 5. The Appendices contain supplementary information.

References

- [1] M. Hand and M. Balas, "Non-linear and linear model based controller design for variable-speed wind turbines," presented at the 3rd ASME/JSME Joint Fluids Engineering Conf., San Francisco, CA, USA, 1999.
- [2] B. Malinga, J. Sneckenberger, and J. Feliachi, "Modeling and control of a wind turbine as a distributed resource," in *Proc. 35th Southeastern Symp. Syst. Theory*, Morgantown, WV, USA, 2003, pp. 108-112.
- [3] J. Svensson and E. Ulen, "The control system of WTS-3 instrumentation and testing," in *Proc. 4th Int. Symp. Wind Energy Systems*, Stockholm, Sweden, 1982, pp. 195-215.
- [4] B. Liebst, "Pitch control system for large-scale wind turbines," *J. of Energy*, vol. 7, no. 2, pp.182-192, March 1983.

- [5] T. Knudsen, P. Andersen, and S. Tiffner-Clausen, "Comparing PI and robust control pitch controllers on a 400KW wind turbine by full scale tests," Department of Control Engineering, Aalborg University, Aalborg, Denmark, Tech. Rep. R-97-4174, 1997.
- [6] S. Mattson, "Modeling and control of large horizontal axis wind power plants," Ph.D. Thesis, Lund Institute of Technology, Lund, Sweden, 1984.
- [7] K. Stol and M. Balas, "Full-state feedback control of a variable-speed wind turbine: A comparison of periodic and constant Gains", *J. of Solar Energy Eng.*, vol. 123, no. 4, pp. 319-326, 2001.
- [8] A. Wright and M. Balas, "Design of state-space-based control algorithms for wind turbine speed regulation," *J. Solar Energy Eng.*, vol. 125, no. 4, pp. 386-395, Nov. 2003.
- [9] R. Chedid, S. Karaki, and C. El-Chamali, "Adaptive fuzzy control for wind-diesel weak power systems," *IEEE Trans. Energy Conversion*, vol. 15, no. 1, pp. 71-78, March 2000.
- [10] M. Prats, J. Carrasco, E. Galvan, J. Sanchez, L. Franquelo and C. Batista, "Improving transition between power optimization and power limitation of variable speed, variable pitch wind turbines using fuzzy control techniques," *Proc. IECON 2000*, Nagoya, Japan, 2000, vol. 3, pp. 1497-1502.
- [11] X. Zhang, W. Wang and Y. Liu, "Fuzzy control of variable speed wind turbine", in *Proc. 6th World Congress on Intelligent Control and Automation*, pp. 3872-3876, Dalian, China, 2006.
- [12] F. Kanellos and N. Hatzargyriou, "A new control scheme for variable speed wind turbines using neural networks," in *Proc. IEEE Power Eng. Soc. Trans. Distrib. Conf.*, New York, NY, 2002, pp. 360-365.
- [13] J. Freeman and M. Balas "An investigation of variable speed horizontal-axis wind turbines using direct model-reference adaptive control" in *Proc. 18th ASME Wind Energy Symp.*, Reno, NV, 1999, pp. 66-76.
- [14] Y. Song, B. Dhinakaran, and X. Bao, "Variable speed control of wind turbines using nonlinear and adaptive algorithms," *J. Wind Eng. Ind. Aerodyn.*, vol. 85, no. 3, pp. 293-308, Apr. 2000.

- [15] K. Johnson, L. Fingersh, M. Balas, and L. Pao, "Methods for increasing region 2 power capture on a variable-speed wind turbine", *J. Solar Energy Eng.*, vol. 126, no. 4, pp. 1092-1100, 2004.
- [16] U. Ozbay, E. Zergeroglu and S. Sivrioglu, "Adaptive backstepping control of variable speed wind turbines," *International Journal of Control*, vol. 81, no. 6, pp. 910-919, Jun. 2008.
- [17] E. Iyasere, M. Salah, D. Dawson and J. Wagner, "Nonlinear robust control to maximize energy capture in a variable speed wind turbine", Proc. of the American Control Conference, pp. 1824-1829, Seattle, WA, USA, Jun. 2008.
- [18] T. Thiringer and J. Luomi, "Comparison of reduced-order dynamic models of induction machines," *IEEE Trans. Power Syst.*, vol. 16, no. 1, pp. 119-126, Feb. 2001.
- [19] A. Tapia, G. Tapia, J. Ostolaza, and J. Saenz, "Modeling and control of a wind turbine driven doubly fed induction generator," *IEEE Trans. Energy Conversion*, vol. 18, no. 2, pp. 194-204, Jun. 2003.
- [20] A. Mullane and M. O'Malley, "Inertial response of induction-machine-based wind turbines" *IEEE Trans. Power Syst.*, vol. 20, no. 3, pp. 1496-1503, Aug. 2005.
- [21] J. Cathey, R. Calvin, and A. Ayoub, "Transient load model of an induction motor," *IEEE Trans. Power Apparatus and Syst.*, vol. 92, no. 4, pp. 1399-1406, Jul. 1973.
- [22] S. Muller and M Deicke "Doubly fed induction generator systems for wind turbines," *IEEE Ind. Appl. Mag.*, pp 26-33, Jun. 2002.
- [23] J. Hu and D. Dawson "Adaptive control of induction motor systems despite rotor resistance uncertainty," *Automatica*, vol. 32, no. 8, pp. 1127-1143, 1996.
- [24] R. Datta and V. Ranganathan, "A simple position-sensorless algorithm for rotor-side field-oriented-control of wound rotor induction machine," *IEEE Trans. Ind. Elect.*, vol. 48, no. 4, pp. 786-793, Aug. 2001.
- [25] R. Pena, J. Clare, and G. Asher, "Doubly fed induction generator using back to back PWM converters and its application to variable-speed wind-energy generation," *IEE Proc. Electr. Power Appl.*, vol. 143, no. 3, pp. 231-241, May 1996.

- [26] R. Marino, S. Peresada, and P. Valigi, "Adaptive input-output linearizing control of induction motors," *IEEE Trans. Automat. Contr.*, vol. 38, no. 2, pp. 208-221, Feb. 1993.
- [27] R. Marino, S. Peresada and P. Tomei, "Global adaptive output feedback control of induction motors with uncertain rotor resistance," *IEEE Trans. Automat. Contr.*, vol. 44, pp. 967-983, May 1999.
- [28] K. Gopakumar, V. Ranganathan, and S. Bhat, "Vector control of induction motor with split phase stator windings," *Conf. Rec. IEEE-IAS Annu. Meeting, Denver, CO, USA*, pp. 569-574, Oct. 1994.
- [29] R. Datta and V. Ranganathan, "Variable-speed wind power generation using doubly fed wound rotor induction machine—a comparison with alternative schemes," *IEEE Trans. Energy Conv.*, vol. 17, no. 3, pp. 414-421, Sept. 2002.
- [30] R. Datta and V. Ranganathan, "Direct Power control of grid-connected wound rotor induction machine without rotor position sensors," *IEEE Trans. Power Elec.*, vol. 16, no. 3, pp. 390-399, May 2001.
- [31] K. Lian, Y. Ouyang and W. Wu, "Realization of maximum power tracking approach for photovoltaic array systems based on T-S fuzzy method," *IEEE International Conf. on Fuzzy Systems*, vol. 1, no. 1, pp. 1874-1879, Jun. 2008.
- [32] K. H. Hussien, I. Muta, T. Hoshino and M. Osakada, "Maximum photovoltaic power tracking: an algorithm for rapidly changing atmospheric conditions," *Proc. IEE-Gener., Transm., Distrib.*, vol. 142, no. 1, pp. 59-64, Jan. 1995.
- [33] Y. Kuo, T. Liang and J. Chen, "Novel maximum-power-point-tracking controller for photovoltaic energy conversion system," *IEEE Trans. Ind. Electron.*, vol. 48, no. 3, pp. 594-601, Jun. 2001.
- [34] T. Kim, H. Ahn, S. Park and Y. Lee, "A novel maximum power point tracking control for photovoltaic power systems under rapidly changing solar radiation," *Proc. IEEE Int. Symp. Ind. Electron.*, vol. 2, no. 1, pp. 1011-1014, 2001.
- [35] R. Leyva, C. Alonso, I. Quenec, A. Cid-Pastor, D. Lagrange and L. Martinez-Salamero, "MPPT of photovoltaic systems using extremum-seeking control," *IEEE Trans. Aero Electron. Syst.*, vol. 42, no. 1, pp. 249-258, Jan. 2001.

- [36] N. Kasa, T. Iida and G. Majumdar, "Robust control for maximum power point tracking in photovoltaic power systems," Proc. Power Conv. Conf., vol. 2, no. 1, pp. 827-832, Apr. 2002.
- [37] S. J. Chiang, K. T. Chang and C. Y. Yen, "Residential photovoltaic energy storage system," IEEE Trans. Ind. Electron., vol. 45, no. 1, pp. 385-394, Jun. 1998.
- [38] C. Hua and J. Lin, "DSP-Based controller application in battery storage of photovoltaic systems," Proc. IEEE IECON Int. Conf. Ind. Electron., Contr. Instrum, vol. 3, pp. 1705-1710, Aug. 1996.
- [39] S. Kim, E. Kim and J. Ahn, "Modeling and control of a grid-connected wind/PV hybrid generation system," Proc. IEEE PES Transmiss. Distrib. Conf. Exhib., pp. 1202-1207, May 2006.
- [40] J. Olila, "A medium power PV-array simulator with robust control strategy," Proc. IEEE Conf. Control Appl., vol. 1, no. 1, pp. 40-45, Sep. 1995.
- [41] F. Valenciaga, P. F. Puleston and P. E. Battaiotto, "Power control of a photovoltaic array in a hybrid electric generation system using sliding mode techniques," IEEE Proc. Control Theory Appl., vol. 148, no. 6, pp. 448-455, Nov. 2001.
- [42] I. S. Kim and M. J. Youn, "Variable-structure observer for solar-array current estimation in a photovoltaic power-generation system," IEEE Proc. Electr. Power Appl., vol. 152, no. 4, Jul. 2005.
- [43] T. Hiyama, S. Kouzuma and T. Imakubo, "Evaluation of neural network based real time maximum power tracking controller for PV systems," IEEE Trans. Energy Conversion, vol. 10, no. 3, pp. 543-548, Sep. 1995.
- [44] ———, "Identification of optimal operating point of PV modules using neural network for real time maximum power tracking control," IEEE Trans. Energy Conversion, vol. 10, no. 2, pp. 360-367, Jun. 1995.
- [45] N. Yadaiah and M. Veerachary, "Adaptive controller for peak power tracking of photovoltaic systems," Syst. Anal. Modelling Simulation, vol. 42, no. 9, pp. 1319-1334, 2002.
- [46] M.M. Saied et al., "Optimal design parameters for a PV array coupled to a DC motor via a DC-DC transformer," IEEE Trans, Energy Conversion, vol. 6, no. 4, pp. 593-598, Dec. 1991.

- [47] S. Alghuwainem, "Matching of a DC motor to a photovoltaic generator using a step-up converter with a current-locked loop," *IEEE Trans. Energy Conversion*, vol. 9, no. 1, pp. 192-198, Mar. 1994.

CHAPTER TWO

NONLINEAR ROBUST CONTROL TO MAXIMIZE ENERGY CAPTURE IN A VARIABLE SPEED WIND TURBINE

In this chapter, a control strategy is developed to regulate the blade pitch angle and rotor speed of a structurally uncertain variable speed wind turbine system. The chapter is organized as follows. In the first section, the control objectives are stated. In the second section, a wind turbine dynamic model is presented. A robust tracking controller is introduced along with the error system dynamics in the next section supported by a Lyapunov-based stability proof. Next, the system nonlinearities are estimated. The reference trajectory generation is discussed in next section, followed by numerical simulation results in the last section.

Problem Statement

The control objective is to maximize the energy captured by a variable speed wind turbine in low to medium wind speeds by tracking a desired pitch angle and rotor speed, in the presence of structurally uncertain wind turbine system nonlinearities. Additionally, the maximization of the energy captured is achieved without the knowledge of the relationship that governs the power capture efficiency of the wind turbine. Instead, an optimization algorithm is developed to seek the unknown optimal blade pitch angle and rotor speed that maximize the energy captured (via the aerodynamic rotor power) while ensuring that the resulting desired trajectories are sufficiently differentiable. The disadvantage of not explicitly knowing the optimal pitch angle and rotor speed a priori is countered by the fact that the optimal rotor speed, and likewise, the optimal pitch angle,

will change as the wind speed changes, which can be accounted for by the optimization algorithm.

Dynamic Model Development

The selected wind turbine model consists of two subsystems: pitch (wind turbine blades and pitch actuator) and drive train (high-speed shaft, gearbox, low-speed shaft and generator) [1]. The aerodynamic rotor power is dependent on the available wind power and the power coefficient. The power coefficient is a function of two variables: the tip-speed ratio (TSR) and the blade pitch angle. The rotor power of the wind turbine,

$P_{\text{aero}}(t) \in \mathbb{R}$, can be defined as

$$P_{\text{aero}} = \frac{1}{2} C_p(\lambda, \beta) \rho A v^3 \quad (2.1)$$

where $\rho \in \mathbb{R}$ is the air density, $A \in \mathbb{R}$ is the rotor swept area, $v(t) \in \mathbb{R}$ is the wind speed, $C_p(\cdot) \in \mathbb{R}$ denotes the power coefficient of the wind turbine, which is assumed to be unknown, $\lambda(t) \in \mathbb{R}$ is the tip-speed ratio, and $\beta(t) \in \mathbb{R}$ represents the blade pitch angle. The tip-speed ratio, $\lambda(t)$, is defined as

$$\lambda = \frac{\omega R}{v} \quad (2.2)$$

where $\omega(t) \in \mathbb{R}$ is the rotor speed and R is the rotor radius. From (2.1) and (2.2), it is clear that there exists an optimal rotor speed ω^* , and blade pitch angle β^* , for a

particular wind speed at which the power capture efficiency is maximum, represented by

$$C_p^{\max}, \text{ where } C_p^{\max} = C_p(\lambda^*, \beta^*).$$

The rotor power, $P_{\text{aero}}(t)$, can also be written as

$$P_{\text{aero}} = \tau_{\text{aero}} \omega \quad (2.3)$$

where $\tau_{\text{aero}}(t) \in \mathbb{R}$ is the aerodynamic torque applied to the rotor by the wind. An

expression for $\tau_{\text{aero}}(t)$ can be derived from (2.1)-(2.3) as

$$\tau_{\text{aero}} = \frac{1}{2} \rho A R \frac{C_p(\lambda, \beta)}{\lambda} v^2 \quad (2.4)$$

Remark 2.1: In (2.1), it is assumed that $C_p(\cdot)$ is unknown, hence $\tau_{\text{aero}}(\cdot)$ is unmeasurable.

The wind turbine model structure can be written as [1]

$$M\ddot{X} + f(\beta, \dot{X}, v) = \tau_c \quad (2.5)$$

where $X(t) \triangleq \begin{bmatrix} \int_{t_0}^t \omega(\sigma) d\sigma & \beta(t) \end{bmatrix}^T \in \mathbb{R}^{2 \times 1}$ are the state variables, $M \in \mathbb{R}^{2 \times 2}$ denotes the

lumped inertia matrix, $f(\cdot) \triangleq [-\tau_{\text{aero}}(\cdot) \quad N(\cdot)]^T \in \mathbb{R}^{2 \times 1}$ represents the system

nonlinearities, $N(\cdot) \in \mathbb{R}$ designates the pitch subsystem nonlinearities, and $\tau_c(t) \in \mathbb{R}^{2 \times 1}$

is the control input torque.

To facilitate the control development process, the following model characteristics are assumed:

A.1: $v(t), \omega(t), \beta(t), \dot{\beta}(t)$ are measurable.

A.2: $v(t)$ is constant or slowly time varying.

A.3: R, A, ρ are known constants.

A.4: $v(t), \dot{v}(t), \ddot{v}(t)$ are bounded.

A.5: $f(\beta, \dot{X}, v, t), \dot{f}(\beta, \dot{X}, \ddot{X}, \dot{v}, t), \ddot{f}(\beta, \dot{X}, \ddot{X}, \ddot{v}, t)$ are bounded provided that

$\beta(t), \dot{X}(t), \ddot{X}(t), \ddot{v}(t)$ are bounded.

A.6: M is a known symmetric, positive definite matrix.

Remark 2.2: $\|f(\beta, \dot{X}, v)\|$ can be upper bounded by a known function such that

$$\|f(\beta, \dot{X}, v)\| \leq \rho_z(\beta, \dot{X}).$$

Error System Development

The control objective is to maximize the aerodynamic rotor power of the wind turbine, $P_{\text{aero}}(t)$, while tracking a desired rotor speed $\omega_d(t) \in \mathbb{R}$ and blade pitch angle $\beta_d(t) \in \mathbb{R}$ such that $\omega(t) \rightarrow \omega_d(t)$ and $\beta(t) \rightarrow \beta_d(t)$ as $t \rightarrow \infty$. To quantify this objective, measurement tracking errors denoted by $e_1(t), e_2(t) \in \mathbb{R}$ are defined as

$$\begin{aligned} e_1(t) &\triangleq \omega_d(t) - \omega(t) \\ e_2(t) &\triangleq \beta_d(t) - \beta(t) \end{aligned} \tag{2.6}$$

Remark 2.3: The variables $\omega_d(t)$ and $\beta_d(t)$ are designed and updated online using a numerical-based two-dimensional optimization algorithm to maximize the rotor power,

$P_{\text{aero}}(t)$, such that at a given wind velocity, $v(t)$, $\beta_d \rightarrow \beta^*$, $\omega_d \rightarrow \omega^*$ hence $P_{\text{aero}} \rightarrow P_{\text{max}}$

where $P_{\text{max}} \triangleq \frac{1}{2} C_p^{\text{max}} \rho A v^3$, and $[\omega^* \ \beta^*]^T$ denotes the set of constants resulting from the

optimum seeking algorithm after convergence. $X_d(t) \triangleq \left[\int_{t_0}^t \omega_d(\sigma) d\sigma, \beta_d(t) \right]^T$ is

designed such that $\beta_d(t), \dot{\beta}_d(t), \ddot{\beta}_d(t), \dddot{\beta}_d(t), \omega_d(t), \dot{\omega}_d(t), \ddot{\omega}_d(t) \in \mathcal{L}_\infty$.

The following filtered tracking error, denoted by $r_2(t) \in \mathbb{R}$, is defined to facilitate the subsequent controller design

$$r_2 \triangleq \dot{e}_2 + \mu e_2, \quad \dot{r}_2 = \ddot{e}_2 + \mu \dot{e}_2 \quad (2.7)$$

where $\mu \in \mathbb{R}$ is a positive constant.

Remark 2.4: Based on the definition of $r_2(t)$ defined in (2.7), standard arguments can be used to prove that if $r_2(t) \in \mathcal{L}_\infty$, then $e_2(t), \dot{e}_2(t) \in \mathcal{L}_\infty$.

After defining a composite error signal denoted by $z(t) = [e_1(t) \ r_2(t)]^T \in \mathbb{R}^2$, taking its time derivative and then pre-multiplying by M , the following expression can be obtained

$$M\dot{z} = M \begin{bmatrix} \dot{e}_1 \\ \dot{e}_2 \end{bmatrix} + M \begin{bmatrix} 0 \\ \mu \dot{e}_2 \end{bmatrix} \quad (2.8)$$

$$M\dot{z} = M\ddot{X}_d - M\ddot{X} + M \begin{bmatrix} 0 \\ \mu \dot{e}_2 \end{bmatrix} \quad (2.9)$$

$$M\dot{z} = M\ddot{X}_d + f(\cdot) - \tau_c + M \begin{bmatrix} 0 \\ \mu \dot{e}_2 \end{bmatrix}. \quad (2.10)$$

$$\tau_c = M\ddot{X}_d + M \begin{bmatrix} 0 \\ \mu \dot{e}_2 \end{bmatrix} + \hat{f}_s(\cdot) + Kz + \frac{\rho_z^2(\cdot)}{\varepsilon} z \quad (2.11)$$

where $\hat{f}_s(\cdot) \triangleq \frac{1}{\tau_1 s + 1} \text{sat}\{\hat{f}(\cdot)\}$, $\hat{f}(\cdot)$ is an estimate of $f(\cdot)$, which will be designed

subsequently in a later section, $K \in \mathbb{R}^+$ is a control gain and $\varepsilon, \tau_1 \in \mathbb{R}^+$ are small

constants, s is the Laplace variable, and $\text{sat}\{\cdot\}$ is the standard saturation function .

Remark 2.5: *The variables $\hat{f}_s(\cdot)$ and $\dot{\hat{f}}_s(\cdot)$ are bounded since the output of a saturation function is always bounded and $1/(\tau_1 s + 1)$ is a proper bounded filter. Thus, it may be*

assumed that $\|\hat{f}_s(\cdot)\| \leq \rho_N$, where $\rho_N \in \mathbb{R}^+$.

Substituting the control torque from (2.11) into the open-loop dynamics of (2.10), results in the following closed-loop error system

$$M\dot{z} = f(\cdot) - \hat{f}_s(\cdot) - Kz - \frac{\rho_z^2(\cdot)}{\varepsilon} z. \quad (2.12)$$

Stability Analysis

Theorem 2.1: *Given the closed loop system of (2.12), all signals remain bounded and the composite error signal $z(t)$ is globally uniformly ultimately bounded (GUUB).*

Proof: A non-negative function, denoted by $V(z(t)) \in \mathbb{R}$, is defined as

$$V = \frac{1}{2} z^T M z. \quad (2.13)$$

Since M is positive-definite and symmetric, the expression in (2.13) can be lower and upper bounded by the following inequalities

$$\lambda_{\min} \|z\|^2 \leq V(z) \leq \lambda_{\max} \|z\|^2 \quad (2.14)$$

where λ_{\min} and λ_{\max} are the minimum and maximum eigenvalues of M respectively.

After taking the time derivative of (2.13), and substituting (2.12), the following expression is obtained

$$\dot{V} = z^T \left[f - \hat{f}_s - Kz - \frac{\rho_z^2}{\varepsilon} z \right] \quad (2.15)$$

$$\dot{V} = -Kz^T z - \frac{\rho_z^2}{\varepsilon} z^T z + z^T f - z^T \hat{f}_s \quad (2.16)$$

From (2.16), using Remarks 2.2 and 2.5, $\dot{V}(t)$ can be upper bounded as

$$\dot{V} \leq -K \|z\|^2 - \frac{\rho_z^2 \|z\|^2}{\varepsilon} + \|z\| \rho_z + \|z\| \rho_N \quad (2.17)$$

if $K = k_1 + k_2$ where $k_1, k_2 \in \mathbb{R}^+$, the nonlinear damping argument [2] may be applied to

(2.17) to obtain

$$\dot{V} \leq -k_1 \|z\|^2 + \varepsilon_o + \rho_z \|z\| \left[1 - \frac{\rho_z \|z\|}{\varepsilon} \right] \quad (2.18)$$

where $\varepsilon_o = \frac{\rho_N^2}{4k_2}$. Using (2.14) and the nonlinear damping argument in (2.18), the

following relationship can be determined

$$\dot{V} \leq -\frac{k_1}{\lambda_{\max}} V + \varepsilon + \varepsilon_o \quad (2.19)$$

From (2.14) and (2.19), the term $\|z(t)\|$ can be upper bounded as

$$\|z(t)\| \leq \sqrt{\beta_0 \exp(-\beta_1 t) + \beta_2 [1 - \exp(-\beta_1 t)]} \quad (2.20)$$

where $\beta_0 \triangleq \frac{\lambda_{\max}}{\lambda_{\min}} \|z(t_0)\|^2$, $\beta_1 \triangleq \frac{k_1}{\lambda_{\max}}$, and $\beta_2 \triangleq \frac{\lambda_{\max}}{k_1 \lambda_{\min}} (\varepsilon + \varepsilon_o)$.

From (2.20), it can be shown that $e_1(t), r_2(t) \in \mathcal{L}_\infty$ thus from Remark 2.4, it is clear that $e_2(t), \dot{e}_2(t) \in \mathcal{L}_\infty$. The expression in (2.6) can be used along with previous boundedness statements to show that $\beta(t), \dot{X}(t) \in \mathcal{L}_\infty$, thus from A.5, it is apparent that $f(\cdot) \in \mathcal{L}_\infty$. The expression in (2.11), can be used along with Remark 2.3 and Remark 2.5 to show that $\tau_c(t) \in \mathcal{L}_\infty$. Standard signal chasing arguments can then be utilized to prove that all signals remain bounded under closed-loop operation. In particular, from (2.12), $\dot{z}(t), \dot{e}_1(t), \ddot{e}_2(t) \in \mathcal{L}_\infty$. Using A.5, it is clear that $\dot{f}(\cdot) \in \mathcal{L}_\infty$. The time derivative of (2.11) can be used along with Remark 2.5 to show that $\dot{\tau}_c(t) \in \mathcal{L}_\infty$. From the time derivative of (2.11), it is clear that $\ddot{X}(t) \in \mathcal{L}_\infty$. Finally it may be concluded that $\ddot{f}(\cdot) \in \mathcal{L}_\infty$ using A.5. The closed-loop system is thus globally uniformly ultimately bounded (GUUB) stable.

Estimation of System Nonlinearities

As previously stated, the main control objective is to maximize the aerodynamic rotor power of a variable speed wind turbine with structurally uncertain system nonlinearities. This model property requires that the system nonlinearities be estimated. The estimate of $f(\cdot)$, denoted by $\hat{f}(\cdot)$, is developed for two reasons:

1. $\hat{f}(\cdot)$ is used as a feed-forward term in the control design, through

$\hat{f}_s(\cdot)$, to reduce the magnitude of the control input torque, $\tau_c(t)$.

2. From Remark 2.1 and (2.3), $P_{\text{aero}}(t)$ is unmeasurable. By utilizing

$\hat{f}(\cdot) = [\hat{\tau}_{\text{aero}}(\cdot) \quad \hat{N}(\cdot)]^T$, an estimate of the captured power, $\hat{P}_{\text{aero}}(t)$, can

be realized where $\hat{P}_{\text{aero}}(t) = \hat{\tau}_{\text{aero}}(t)\omega(t)$.

Now consider the two systems

$$M\ddot{X} = \tau_c - f(\beta, \dot{X}, v), \quad M\ddot{\hat{X}} = \tau_c - \hat{f}(\cdot) \quad (2.21)$$

where $\hat{X}(t) \in \mathbb{R}^{2 \times 1}$ denotes the estimate of the states, and $\hat{f}(\cdot)$ is the estimate of $f(\cdot)$.

The objective of the estimator is to track the system nonlinearities $f(\cdot)$ such that

$\hat{f}(\cdot) \rightarrow f(\cdot)$ as $t \rightarrow \infty$. To quantify this objective, the observation errors,

$\dot{\tilde{X}}(t), \tilde{f}(t) \in \mathbb{R}^2$ are defined as

$$\dot{\tilde{X}} = \dot{\hat{X}} - \dot{X}, \quad \tilde{f} = \hat{f} - f. \quad (2.22)$$

The filtered observation error, denoted by $r(t) \in \mathbb{R}^{2 \times 1}$, is defined to facilitate the subsequent design

$$r = \ddot{\tilde{X}} + \Delta \dot{\tilde{X}} \quad (2.23)$$

where $\Delta \in \mathbb{R}^+$ is a constant. After taking the time derivative of (2.23) and pre-multiplying by M , it may be shown that

$$M\dot{r} = M\ddot{\tilde{X}} + \Delta M\dot{\tilde{X}} = -\dot{\hat{f}} + \dot{f} + \Phi - \dot{\tilde{X}} \quad (2.24)$$

where $\Phi(\cdot) = \Delta M\ddot{\tilde{X}} + \dot{\tilde{X}}$.

Remark 2.6: The auxiliary signal $\Phi(\cdot)$ can be upper bounded such that $\|\Phi(\cdot)\| \leq \bar{\rho}_N \|\bar{z}\|$

where $\bar{z}(t) = [\tilde{\omega}(t), r(t)]^T \in \mathbb{R}^3$ and $\bar{\rho}_N \in \mathbb{R}^+$ is a constant.

Based on the structure of (2.24) as well as the subsequent stability analysis, the following implementable continuous estimator is proposed to achieve the stated estimator objectives

$$\dot{\hat{f}} = (k + \Delta)r + \rho_0 \operatorname{sgn}(\dot{\tilde{X}}) \quad (2.25)$$

where $k, \rho_0 \in \mathbb{R}^+$ are control gains.

Before presenting the stability analysis, the following lemma will be introduced and later invoked.

Lemma 2.1: Let the auxiliary function $L(t) \in \mathbb{R}$ be defined as

$$L \triangleq r^T \left(\dot{f} - \rho_0 \operatorname{sgn}(\dot{\tilde{X}}) \right). \quad (2.26)$$

If the control gain ρ_o is selected to satisfy the sufficient condition

$\rho_o > \|\dot{f}(\cdot)\| + \frac{\|\ddot{f}(\cdot)\|}{\Delta}$, then $\int_{t_0}^t L(\tau) d\tau \leq \zeta_o$ where the positive constant $\zeta_o \in \mathbb{R}$ is

$$\zeta_o \triangleq \rho_o \left\| \dot{\tilde{X}}(t_0) \right\| + \dot{\tilde{X}}^T(t_0) \dot{f}(t_0). \quad (2.27)$$

Proof: Refer to Appendix A.

Theorem 2.2: The estimator in (2.25) ensures that asymptotic tracking is obtained, in the sense that $\left\| \dot{\tilde{X}}(t) \right\|, \left\| \ddot{\tilde{X}}(t) \right\|, \left\| r(t) \right\| \rightarrow 0$ as $t \rightarrow \infty$.

Proof: Define an auxiliary function $P(t) \in \mathbb{R}$ as follows

$$P = \zeta_o - \int L(\tau) d\tau \quad (2.28)$$

where $\zeta_o(t), L(t)$ have been defined in Lemma 2.1. Since from the proof of Lemma 2.1,

$P(t)$ is non-negative, the following non-negative Lyapunov function, denoted by $V_1(t)$

is defined as

$$V_1(t) = \frac{1}{2} \dot{\tilde{X}}^T \dot{\tilde{X}} + \frac{1}{2} r^T M r + P. \quad (2.29)$$

After taking the time derivative of (2.29), utilizing the definitions in (2.23), (2.24), (2.26), (2.28), and rearranging terms, the following expression is obtained

$$\dot{V}_1 = -\Delta \dot{\tilde{X}}^T \dot{\tilde{X}} - r^T \hat{f} + r^T \Phi + r^T \rho_o \operatorname{sgn}(\dot{\tilde{X}}). \quad (2.30)$$

After substituting (2.25) and performing simple algebraic manipulations, $\dot{V}_1(t)$ can be upper bounded by

$$\dot{V}_1 \leq \Delta \|\bar{z}\|^2 + \left[\|r\| \bar{\rho}_N \|\bar{z}\| - k \|r\|^2 \right] \quad (2.31)$$

where $\bar{z}(t)$ is a composite error vector previously defined in (2.24). Applying the nonlinear damping argument [2] to the bracketed term results in

$$\dot{V}_1 \leq - \left[\Delta - \frac{\bar{\rho}_N^2}{4k} \right] \|\bar{z}\|^2. \quad (2.32)$$

From (2.32), it is possible to state that

$$\dot{V}_1 \leq -\gamma \|\bar{z}\|^2 \quad \text{for } k > \frac{\bar{\rho}_N^2}{4\Delta} \quad (2.33)$$

where $\gamma \in \mathbb{R}$ is a positive constant. From (2.29) and (2.33), it is clear that $\bar{z}(t) \in \mathcal{L}_\infty$.

From the definition of $\bar{z}(t)$, it is clear that $\dot{\bar{X}}(t), r(t) \in \mathcal{L}_\infty$. From (2.25), it is clear that

$\hat{f}(\cdot) \in \mathcal{L}_\infty$. Using standard signal chasing arguments, it can be shown that all the signals

in the closed-loop system remain bounded. In particular, from (2.24), it may be

concluded that $\dot{r}(t) \in \mathcal{L}_\infty$. Next, one can deduce that $\dot{\bar{z}}(t) \in \mathcal{L}_\infty$. After employing a

corollary to Barbalat's Lemma [3], it can be shown that $\|\bar{z}(t)\| \rightarrow 0$ as $t \rightarrow \infty$. From the

definition of $\bar{z}(t)$, it is clear that $\dot{\bar{X}}(t), r(t) \rightarrow 0$ as $t \rightarrow \infty$. From (2.23), it may be noted

that $\ddot{\bar{X}}(t) \rightarrow 0$ as $t \rightarrow \infty$. From (2.21), the following relationship can be obtained

$$M\ddot{\bar{X}} = f - \hat{f} = -\tilde{f}. \quad (2.34)$$

From (2.34), $\tilde{f}(t) \rightarrow 0$ as $t \rightarrow \infty$, which implies that $\hat{\tau}_{aero}(t) \rightarrow \tau_{aero}(t)$.

Trajectory Generator

In Remark 3, it was assumed that a composite set of desired trajectories denoted by $\xi_d(t) = [\omega_d(t) \quad \beta_d(t)]^T$ can be generated such that $\xi_d(t), \dot{\xi}_d(t), \ddot{\xi}_d(t), \ddot{\beta}_d(t) \in \mathcal{L}_\infty$ and $\xi_d \rightarrow \xi^*$ where ξ^* is an unknown set of constants that maximizes the aerodynamic rotor power $P_{\text{aero}}(t)$. As stated previously, $P_{\text{aero}}(t)$ is unmeasurable, thus, the estimated captured power $\hat{P}_{\text{aero}} = \hat{\tau}_{\text{aero}}\omega$ can be used instead. The optimum seeking algorithm used in this study is the Powell's method. Powell's method only requires measurement of the output function $\hat{P}_{\text{aero}}(t)$ and an initial guess (not required to be close to the value of ξ^*). Powell's method can then find ξ^* by performing a series of one dimensional line maximizations (using Brent's method) with convergence due to the non-trivial choice of search directions [4] (*new directions are calculated using the extended parallel subspace property to avoid linear dependence*).

To ensure that $\xi_d(t), \dot{\xi}_d(t), \ddot{\xi}_d(t), \ddot{\beta}_d(t) \in \mathcal{L}_\infty$, a filter based form of Powell's method is used, wherein at each iteration, $\xi_d(k)$ is passed through a set of third order stable and proper low pass filters to generate continuous bounded signals for $\xi_d(t), \dot{\xi}_d(t), \ddot{\xi}_d(t), \ddot{\beta}_d(t)$. The filters shown in (2.35)-(2.38) are used in this study, where $\zeta_1, \zeta_2, \zeta_3, \zeta_4 \in \mathbb{R}^+$ are filter constants. The optimization algorithm waits until certain error thresholds are met before making the next guess (if $\|\xi_d(t) - \xi_d(k)\| \leq \bar{e}_1$, $|\tilde{f}(\cdot)| \leq \bar{e}_2$ and $\|\xi(t) - \xi_d(t)\| \leq \bar{e}_3$ then $k = k + 1$ where $e_1, e_2, e_3 \in \mathbb{R}^+$ are constants and $k = \mathbb{Z}^+$).

$$\xi_d(t) = \frac{\zeta_1}{s^3 + \zeta_2 s^2 + \zeta_3 s + \zeta_4} \xi_d(k) \quad (2.35)$$

$$\dot{\xi}_d(t) = \frac{\zeta_1 s}{s^3 + \zeta_2 s^2 + \zeta_3 s + \zeta_4} \xi_d(k) \quad (2.36)$$

$$\ddot{\xi}_d(t) = \frac{\zeta_1 s^2}{s^3 + \zeta_2 s^2 + \zeta_3 s + \zeta_4} \xi_d(k) \quad (2.37)$$

$$\ddot{\beta}_d(t) = \frac{\zeta_1 s^3}{s^3 + \zeta_2 s^2 + \zeta_3 s + \zeta_4} \beta_d(k) \quad (2.38)$$

Simulation Results

A numerical simulation is presented to illustrate the performance of the controller introduced in (2.11), and to demonstrate the numerical-based optimum seeking reference trajectory generator. The system model in (2.5) corresponded to a small turbine and was assumed to have the following system nonlinearities

$$f(\cdot) = \left[-\frac{1}{2} \rho A \frac{C_p(\lambda, \beta)}{\omega} v^3 \quad 0 \right]^T \quad (2.39)$$

The model parameters are listed in Appendix B. The desired and actual rotor speeds, $\omega_d(t)$ and $\omega(t)$, respectively, are shown in Fig. 2.1. It is clear that $\omega(t)$ successfully tracks $\omega_d(t)$. Similarly, it is clear that $\beta(t)$ successfully tracks $\beta_d(t)$ as shown in Fig. 2.2. The power coefficient function $C_p(\lambda, \beta)$, illustrated in Fig. 2.3, was obtained using blade-element momentum theory in [5]. For this case, $C_p^{\max} = 0.4405$ at

$[\lambda^* = 8 \quad \beta^* = 2.4]$ which according to (2.2), corresponds to $[\omega^* = 6 \quad \beta^* = 2.4]$. The numerical-based optimum seeking algorithm converged to $[\omega^* = 6.075 \quad \beta^* = 2.3]$ as shown in Figs. 2.1 and 2.2. In Fig. 2.4, the maximum simulated power coefficient $C_p(t)$, converges to $C_p^{\max} = 0.4401$. After analysis, the following four conclusions can be made. First, From Figs. 2.1 and 2.2, it can be concluded that $\omega(t) \rightarrow \omega_d(t)$, $\beta(t) \rightarrow \beta_d(t)$ and $\omega_d(t) \rightarrow \omega^*$, $\beta_d(t) \rightarrow \beta^*$, thus $\omega(t) \rightarrow \omega^*$ and $\beta(t) \rightarrow \beta^*$, which fulfills the stated control objective. Second, the results of the optimum seeking algorithm were within five percent of the nominal optimum blade pitch angle and rotor speed. Next, the tracking errors, $e_1(t), e_2(t)$, for both subsystems settle to a neighborhood of $\pm 5 \times 10^{-6}$ around zero after 400 seconds. Finally, the control input $\tau(t)$ is bounded as shown in Fig. 2.5. Overall, the control strategy proposed in this study produced favorable results and demonstrates that at low to medium speeds, it is possible to attain optimal power capture efficiency in variable speed and pitch wind turbines in the presence of structural uncertainty in the form of unknown system nonlinearities. Additionally the robustness of the control strategy allows for varying wind speeds in obtaining the global maximal power efficiency.

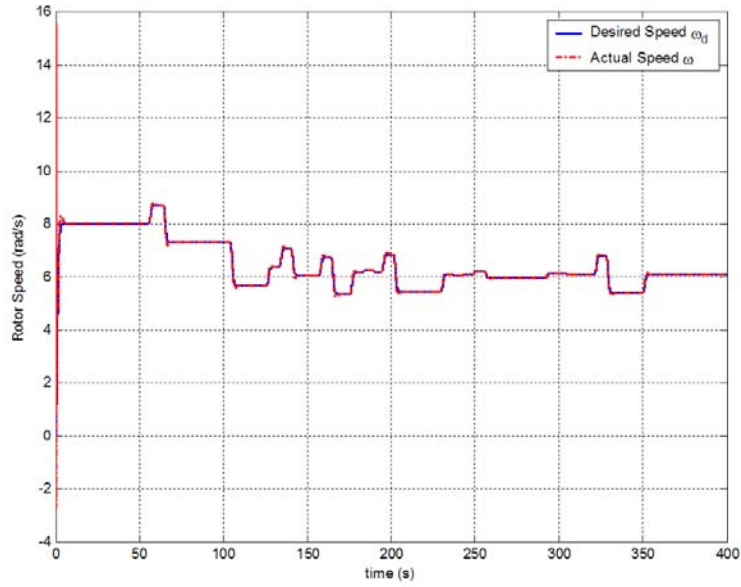


Figure 2.1: Desired rotor speed $\omega_d(t)$ and actual rotor speed $\omega(t)$

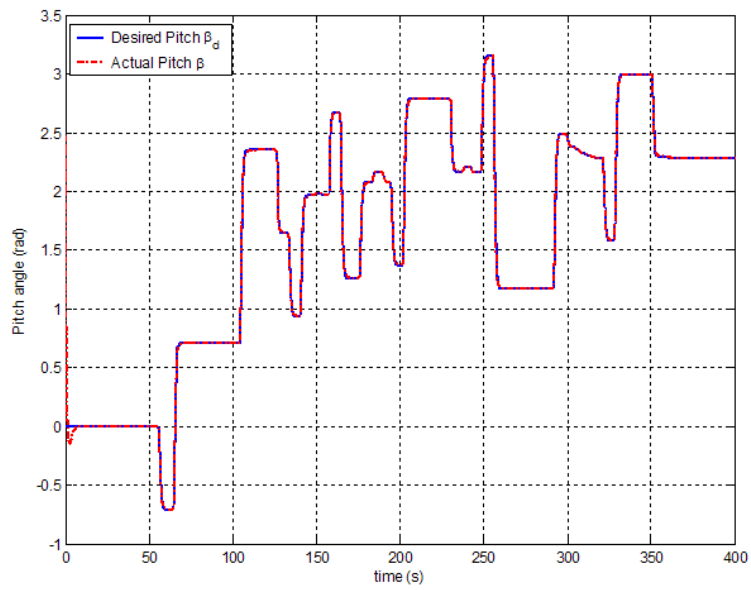


Figure 2.2: Desired blade pitch $\beta_d(t)$ and actual blade pitch $\beta(t)$

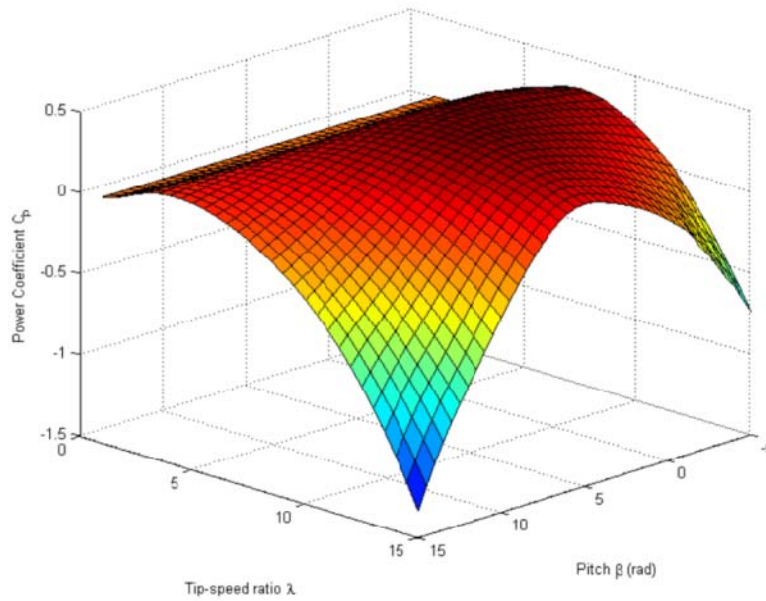


Figure 2.3: Power coefficient function C_p versus tip-speed ratio λ , and blade pitch angle β , for the simulated wind turbine

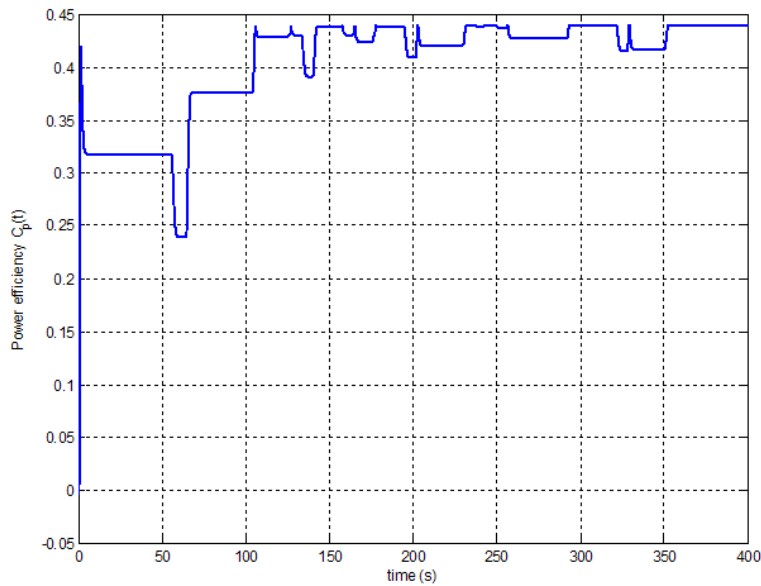


Figure 2.4: Maximum rotor power coefficient $C_p(t)$ resulting from the numerical optimization algorithm

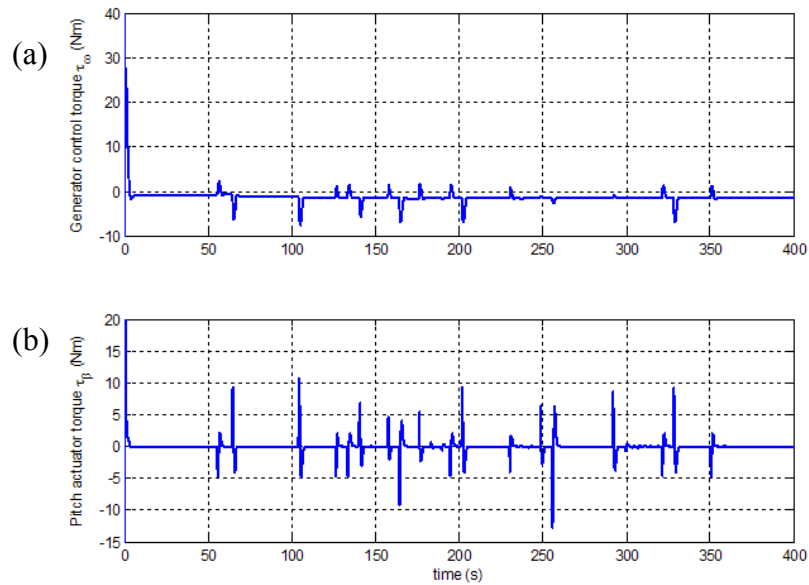


Figure 2.5: Simulated control torque for (a) drive train subsystem, $\tau_{\omega}(t)$ and pitch subsystem $\tau_{\beta}(t)$

References

- [1] K. Johnson, L. Pao, M. Balas, and L. Fingersh, "Control of variable-speed wind turbines: Standard and adaptive techniques for maximizing energy capture", IEEE Control Syst. Mag., vol. 26, no. 3, pp. 70-81, June 2006.
- [2] P. Kokotovic, "The joy of feedback: nonlinear and adaptive," IEEE Control Syst. Mag., vol. 12, no. 3, pp. 7-17, June 1992.
- [3] J. Slotine and W. Li, Applied Nonlinear Control, Englewood Cliffs, NJ: Prentice Hall, 1991.
- [4] G. Reklaitis, A. Ravindran, and K. Ragsdell, Engineering Optimization, Hoboken, NJ: John Wiley & Sons, 1983, pp. 41-130.
- [5] NWTTC Design Codes (WT_Perf by Marshall Buhl), <http://wind.nrel.gov/designcodes/simulators/wtperf/>, Aug. 1, 2007.

CHAPTER THREE

NONLINEAR ROBUST CONTROL TO MAXIMIZE ENERGY CAPTURE IN A VARIABLE SPEED WIND TURBINE USING AN INDUCTION GENERATOR

In this chapter, a control strategy is developed to regulate the rotor speed of a small variable speed wind turbine system coupled to an induction generator. The chapter is organized as follows. In the first section, the control objectives are stated. In the second section, the system model and problem statement are mathematically formulated. A robust speed tracking controller is designed and a supporting stability analysis is presented in the next section. Next, an observer is designed to estimate the system nonlinearities. This estimate of the system nonlinearities is used to generate the rotor speed reference trajectory in the next section, and is followed by numerical simulation results in last section.

Problem Statement

The control objective is to maximize the energy captured by a wind turbine coupled to a doubly-fed induction generator for low to medium air speeds by tracking a desired rotor speed in the presence of system nonlinearities and structural uncertainty. Additionally, the maximization of the energy captured is achieved without the knowledge of the relationship that governs the power capture efficiency of the wind turbine. Instead, an optimization algorithm is developed to seek the unknown optimal rotor speed that maximizes the energy captured (via the aerodynamic rotor power), at a particular blade pitch angle and wind speed, while ensuring that the resulting trajectory is sufficiently differentiable. The problem of not explicitly knowing the rotor speed *a priori* is

countered by the fact that the optimal rotor speed will change as the wind speed changes which may be accommodated for by choosing the right optimization algorithm.

Nomenclature

β	Blade pitch angle (rad).
C_p	Power capture efficiency.
I	Current (A).
L	Inductance (H).
λ	Tip speed ratio.
M	Mutual inductance (H).
M_m	Moment of inertia (kg.m ²).
n_p	Number of generator pole pairs.
ω	Rotor angular velocity (rad/s).
$\bar{\Psi}, \Psi$	Flux Linkage (Wb).
P	Power (W).
R	Resistance (Ω).
R_a	Blade radius.
ρ_a	Air density (kg/m ³).
τ_{em}	Electromagnetic torque (N.m).
v	Wind velocity (m/s ²)
V_r	Rotor Voltage (V)
V_s	Stator (Grid Side) Voltage (V)

Subscripts and Superscripts

*	Optimal value
a, b	Fixed stator frame component
d	Desired value
max	Maximum value
r, s	Rotor, stator

System Model

The wind turbine model consists of a wind rotor, drive shaft and an internal induction generator. The aerodynamic rotor power captured by the wind turbine is dependent on the available wind power and the power coefficient, C_p , which is a function of the tip-speed ratio (TSR) $\lambda(t) \in \mathbb{R}$, and the blade pitch angle, $\beta \in \mathbb{R}$. The rotor power of the wind turbine, $P_{\text{aero}}(t) \in \mathbb{R}$, can be defined as

$$P_{\text{aero}} = \frac{1}{2} C_p \rho_a \pi R_a^2 v^3 \quad (3.1)$$

where $C_p(\lambda, \beta) \in \mathbb{R}$ is assumed to be unknown. The tip-speed ratio, $\lambda(t)$, is defined as

$$\lambda = \frac{\omega R_a}{v}. \quad (3.2)$$

From (3.1) and (3.2), it can be inferred that there exists a constant optimal rotor speed, ω^* , for a particular wind speed, $v(t)$, and blade pitch angle, β , at which the power capture efficiency, and thus the aerodynamic rotor power is maximum, with

$$P_{\text{max}} \triangleq \frac{1}{2} C_p^{\text{max}} \rho_a \pi R_a^2 v^3, \quad C_p^{\text{max}} = C_p(\lambda^*, \beta) \quad \text{and} \quad \lambda^* = \frac{\omega^* R_a}{v} \quad [1].$$

The rotor power, $P_{\text{aero}}(t)$, can also be written as

$$P_{\text{aero}} = \tau_{\text{aero}} \omega \quad (3.3)$$

where $\tau_{\text{aero}}(t) \in \mathbb{R}$ is the aerodynamic torque applied to the rotor by the wind. An expression for $\tau_{\text{aero}}(t)$ can be derived from (3.1)-(3.3) as

$$\tau_{\text{aero}} = \frac{1}{2} \rho_a \pi R_a^3 \frac{C_p}{\lambda} v^2. \quad (3.4)$$

Remark 3.1: In (3.1), it is assumed that $C_p(\cdot)$ is unknown which implies that $\tau_{\text{aero}}(t)$ and $P_{\text{aero}}(t)$ are unmeasurable.

Mechanical Subsystem Dynamics

The mechanical subsystem describes the rotor dynamics of the variable speed wind turbine and is assumed to be of the form

$$M_m \dot{\omega} + f = \tau_{em} \quad (3.5)$$

where $\dot{\omega}(t)$ is the rotor acceleration, and $f(\omega, v) \triangleq -\tau_{\text{aero}}(t)$ represents the system nonlinearities.

Electrical Subsystem Dynamics

The standard induction machine model can be found in [2]. The model utilized in this paper is the transformed nonlinear induction machine model in the stator fixed a - b reference frame with the assumptions of equal mutual and auto inductances, and a linear magnetic circuit [3]. The electrical dynamics of the internal induction generator can be described by the following dynamic equations:

$$\dot{\bar{\Psi}}_s = -R_s \bar{I}_s + V_s \quad (3.6)$$

$$\dot{\bar{\Psi}}_r = -R_r \bar{I}_r + n_p \omega J \bar{\Psi}_r + \bar{V}_r \quad (3.7)$$

$$\bar{I}_s = \kappa_1 \bar{\Psi}_s - \kappa_2 \bar{\Psi}_r \quad (3.8)$$

$$\bar{I}_r = \kappa_1 \bar{\Psi}_r - \kappa_2 \bar{\Psi}_s \quad (3.9)$$

$$\tau_{em} = \alpha \bar{\Psi}_s^T J \bar{\Psi}_r \quad (3.10)$$

$$J = \begin{bmatrix} 0 & -1 \\ 1 & 0 \end{bmatrix}, \quad \alpha = n_p \kappa_2 \quad (3.11)$$

where $\bar{\Psi}_s = [\bar{\Psi}_{s_a}, \bar{\Psi}_{s_b}]^T$, $\bar{\Psi}_r = [\bar{\Psi}_{r_a}, \bar{\Psi}_{r_b}]^T$, $\bar{V}_s = [\bar{V}_{s_a}, \bar{V}_{s_b}]^T$, $\bar{V}_r = [\bar{V}_{r_a}, \bar{V}_{r_b}]^T$,

$\bar{I}_s = [\bar{I}_{s_a}, \bar{I}_{s_b}]^T$, $\bar{I}_r = [\bar{I}_{r_a}, \bar{I}_{r_b}]^T \in \mathbb{R}^2$. In (3.8) and (3.9), κ_1 and κ_2 are constants related to

the motor parameters, and are given explicitly by

$$\kappa_1 = \frac{L_s}{L_s^2 - M^2}, \kappa_2 = \frac{M}{L_s^2 - M^2}. \quad (3.12)$$

To facilitate the control development, the following model characteristics are assumed:

Assumption 1: The parameters L_s , M , M_m , n_p , R_a , R_r , R_s , β and ρ_a are known constants.

Assumption 2: $\omega(t)$, $\bar{I}_s(t)$, $\bar{I}_r(t)$, $V_s(t)$, and $v(t)$ are measurable.

Assumption 3: $v(t)$ is constant or slowly time varying (*i.e.*, $\dot{v} \cong 0$).

Assumption 4: $v(t)$, $\dot{v}(t)$, $\ddot{v}(t)$ are bounded.

Assumption 5: As a consequence of the fact that $\tau_{aero}(t)$ is unknown, $f(\omega, v)$,

introduced in (3.5) is also unknown.

Assumption 6: The variables, $f(\cdot)$, $\dot{f}(\cdot)$, $\ddot{f}(\cdot)$ are bounded provided that $\omega(t)$, $\dot{\omega}(t)$, $\ddot{\omega}(t)$ are bounded.

Remark 3.2: $f(\omega, v)$ can be upper bounded by a known function such that

$|f(\omega, v)| \leq \rho(\omega)$ where $\rho(\omega)$ is continuously differentiable for all $\omega(t) > 0$.

Electrical Subsystem Transformation

An auxiliary control input $\omega_s(t)$ is injected into the electrical subsystem dynamics via time-varying coordinate transformation [4] as follows

$$\begin{aligned} \Psi_s &\triangleq T\bar{\Psi}_s, & I_s &\triangleq T\bar{I}_s, & V_r &\triangleq T\bar{V}_r \\ \Psi_r &\triangleq T\bar{\Psi}_r, & I_r &\triangleq T\bar{I}_r, & V_s &\triangleq T\bar{V}_s \end{aligned} \quad (3.13)$$

where $T(t) \in \mathbb{R}^{2 \times 2}$ is defined as

$$T \triangleq \begin{bmatrix} \cos(\varepsilon_0) & \sin(\varepsilon_0) \\ -\sin(\varepsilon_0) & \cos(\varepsilon_0) \end{bmatrix} \quad (3.14)$$

where $\dot{\varepsilon}_0 = \omega_s$. It should be noted that $T(t)$ satisfies $T^{-T}JT^{-1} = J$.

The overall dynamics of the induction generator can then be given by the following fifth order model:

$$M_m \dot{\omega} + f = \tau_{em} \quad (3.15)$$

$$\dot{\Psi}_s = -R_s \kappa_1 \Psi_s + R_s \kappa_2 \Psi_r - J \Psi_s \omega_s + V_s \quad (3.16)$$

$$\dot{\Psi}_r = V_r - R_r \kappa_1 \Psi_r + R_r \kappa_2 \Psi_s + n_p \omega J \Psi_r - J \Psi_r \omega_s \quad (3.17)$$

$$\tau_{em} = \alpha \Psi_s^T J \Psi_r \quad (3.18)$$

$$I_s = \kappa_1 \Psi_s - \kappa_2 \Psi_r \quad (3.19)$$

$$I_r = \kappa_1 \Psi_r - \kappa_2 \Psi_s \quad (3.20)$$

where $\Psi_s = [\Psi_{s_1}, \Psi_{s_2}]^T$, $\Psi_r = [\Psi_{r_1}, \Psi_{r_2}]^T$, $V_r = [V_{r_1}, V_{r_2}]^T$, $V_s = [V_{s_1}, V_{s_2}]^T$.

Controller Design

The objective is to maximize the aerodynamic rotor power of the wind turbine, $P_{\text{aero}}(t)$, by tracking a desired rotor speed $\omega_d(t) \in \mathbb{R}$ such that $\omega(t) \rightarrow \omega_d(t)$ as $t \rightarrow \infty$. This is achieved in turn by tracking a desired electromagnetic torque, $\tau_d(t) \in \mathbb{R}$, a desired stator flux $\Psi_s^d(t) \in \mathbb{R}^{2 \times 1}$, and a desired rotor flux $\Psi_r^d(t) \in \mathbb{R}^{2 \times 1}$ such that $\Psi_s(t) \rightarrow \Psi_s^d(t)$, $\Psi_r(t) \rightarrow \Psi_r^d(t)$, and $\tau_{em}(t) \rightarrow \tau_d(t)$ where

$$\Psi_s^d = [\Psi_{s_1}^d, 0]^T \quad \Psi_r^d = [\Psi_{r_1}^d, \Psi_{r_2}^d]^T \quad (3.21)$$

$$\tau_d \triangleq \alpha (\Psi_s^d)^T J \Psi_r^d. \quad (3.22)$$

Remark 3.3: *The desired rotor speed, $\omega_d(t)$, is designed online using a numerical-based optimization algorithm, as shown in a later section, to maximize the rotor power $P_{\text{aero}}(t)$ at a particular blade pitch angle, β , and wind velocity, $v(t)$, such that $\omega_d(t) \rightarrow \omega^*$, where the optimal speed, ω^* , is the result of the optimum seeking algorithm after*

convergence, hence $P_{\text{aero}}(t) \rightarrow P_{\text{max}}$ if $\omega(t) \rightarrow \omega_d(t)$. Additionally, $\omega_d(t)$ is designed such that $\omega_d(t), \dot{\omega}_d(t), \ddot{\omega}_d(t) \in \mathcal{L}_\infty$.

Remark 3.4: The desired rotor flux, $\Psi_{s_1}^d(t)$, is designed such that $\Psi_{s_1}^d(t) > 0$,

$\Psi_{s_1}^d(t), \dot{\Psi}_{s_1}^d(t), \ddot{\Psi}_{s_1}^d(t) \in \mathcal{L}_\infty$, and power loss in the system is minimized, as shown in Appendix C.

Remark 3.5: To ensure equality in (3.22), $\Psi_{r_2}^d(t)$ is designed such that $\Psi_{r_2}^d = \frac{-\tau_d}{\alpha \Psi_{s_1}^d}$.

Error System Development

To quantify the control objective, rotor speed, stator flux and rotor flux tracking errors, denoted by $e(t) \in \mathbb{R}$, $\eta_s(t), \eta_r(t) \in \mathbb{R}^{2 \times 1}$, respectively, are defined as

$$e \triangleq \omega_d - \omega \quad (3.23)$$

$$\eta_s = \begin{bmatrix} \eta_{s_1} \\ \eta_{s_2} \end{bmatrix} = \begin{bmatrix} \Psi_{s_1}^d \\ 0 \end{bmatrix} - \begin{bmatrix} \Psi_{s_1} \\ \Psi_{s_2} \end{bmatrix} \quad (3.24)$$

$$\eta_r = \begin{bmatrix} \eta_{r_1} \\ \eta_{r_2} \end{bmatrix} = \begin{bmatrix} \Psi_{r_1}^d \\ \Psi_{r_2}^d \end{bmatrix} - \begin{bmatrix} \Psi_{r_1} \\ \Psi_{r_2} \end{bmatrix} \quad (3.25)$$

where $\eta_{s_1}(t), \eta_{s_2}(t), \eta_{r_1}(t), \eta_{r_2}(t) \in \mathbb{R}$.

From the definition of the tracking error in (3.23), and subsystem dynamics in (3.5), a rotor speed open-loop error system is obtained as follows

$$M_m \dot{e} = M_m \dot{\omega}_d + f - \tau_{em}. \quad (3.26)$$

Substituting in (3.18) and adding and subtracting (3.22) to the right hand side of (3.26) results in

$$M_m \dot{e} = M_m \dot{\omega}_d + f - \tau_d + \alpha \left[\left(\Psi_s^d \right)^T J \Psi_r^d - \Psi_s^T J \Psi_r \right]. \quad (3.27)$$

Substituting in (3.24) and (3.25) into (3.27), and performing simple algebraic manipulations, results in

$$\begin{aligned} M_m \dot{e} = & M_m \dot{\omega}_d + f - \tau_d - \alpha \Psi_{s_1}^d \eta_{r_2} + \alpha \Psi_{r_1}^d \eta_{s_2} \\ & - \alpha \Psi_{r_2}^d \eta_{s_1} - \alpha \eta_{s_2} \eta_{r_1} + \alpha \eta_{s_1} \eta_{r_2}. \end{aligned} \quad (3.28)$$

Similarly, the stator and rotor flux open-loop error systems are developed as follows

$$\begin{aligned} \begin{bmatrix} \dot{\eta}_{s_1} \\ \dot{\eta}_{s_2} \end{bmatrix} = & \begin{bmatrix} \dot{\Psi}_{s_1}^d \\ 0 \end{bmatrix} + R_s \kappa_1 \begin{bmatrix} \Psi_{s_1}^d \\ 0 \end{bmatrix} - R_s \kappa_1 \begin{bmatrix} \eta_{s_1} \\ \eta_{s_2} \end{bmatrix} + R_s \kappa_2 \begin{bmatrix} \eta_{r_1} \\ \eta_{r_2} \end{bmatrix} \\ & - R_s \kappa_2 \begin{bmatrix} \Psi_{r_1}^d \\ \Psi_{r_2}^d \end{bmatrix} + \begin{bmatrix} 0 \\ \Psi_{s_1}^d \end{bmatrix} \omega_s + \begin{bmatrix} \eta_{s_2} \\ -\eta_{s_1} \end{bmatrix} \omega_s - \begin{bmatrix} V_{s_1} \\ V_{s_2} \end{bmatrix} \end{aligned} \quad (3.29)$$

$$\begin{aligned} \begin{bmatrix} \dot{\eta}_{r_1} \\ \dot{\eta}_{r_2} \end{bmatrix} = & \begin{bmatrix} \dot{\Psi}_{r_1}^d \\ \dot{\Psi}_{r_2}^d \end{bmatrix} + R_r \kappa_2 \begin{bmatrix} \eta_{s_1} \\ \eta_{s_2} \end{bmatrix} - R_r \kappa_2 \begin{bmatrix} \Psi_{s_1}^d \\ 0 \end{bmatrix} + R_r \kappa_1 \begin{bmatrix} \Psi_{r_1}^d \\ \Psi_{r_2}^d \end{bmatrix} - R_r \kappa_1 \begin{bmatrix} \eta_{r_1} \\ \eta_{r_2} \end{bmatrix} \\ & + n_p \omega \begin{bmatrix} -\eta_{r_2} \\ \eta_{r_1} \end{bmatrix} - n_p \omega \begin{bmatrix} -\Psi_{r_2}^d \\ \Psi_{r_1}^d \end{bmatrix} - \begin{bmatrix} V_{r_1} \\ V_{r_2} \end{bmatrix} + \begin{bmatrix} -\Psi_{r_2}^d \\ \Psi_{r_1}^d \end{bmatrix} \omega_s - \begin{bmatrix} -\eta_{r_2} \\ \eta_{r_1} \end{bmatrix} \omega_s \end{aligned} \quad (3.30)$$

where (3.16), (3.17), and the time derivatives of (3.24) and (3.25) were utilized.

Control Input Design

The control inputs will be designed based on the subsequent stability analysis as well as the structure of the open loop error systems in (3.28)-(3.30).

The desired torque trajectory, $\tau_d(t)$ is designed to be

$$\tau_d = Ke + \frac{\rho^2(\omega)e}{\varepsilon} + M_m \dot{\omega}_d - \hat{f}_s \quad (3.31)$$

where $\hat{f}_s(\cdot) \triangleq \frac{1}{\sigma s + 1} \text{sat}\{\hat{f}(\cdot)\}$, $\text{sat}\{\cdot\}$ is the saturation function, $\hat{f}(\cdot)$ is an estimate of $f(\cdot)$ which will be designed in Section 4, $s \in \mathbb{C}$ is the Laplace variable, $K \in \mathbb{R}^+$ is a control gain, $\varepsilon, \sigma \in \mathbb{R}^+$ are constants and $\rho(\omega)$ was previously defined in Remark 3.2.

Remark 3.6: Since $\frac{1}{\sigma s + 1}$ is a proper bounded filter and the output of the saturation

function is always bounded then it can be concluded that $\hat{f}_s(\cdot), \dot{\hat{f}}_s(\cdot) \in \mathcal{L}_\infty$. Thus, it may

be concluded that $|\hat{f}_s(\cdot)| \leq \rho_s$ where $\rho_s \in \mathbb{R}^+$.

The first entry of the desired rotor flux, $\Psi_{r_1}^d(t)$, is designed to be

$$\Psi_{r_1}^d = \frac{1}{R_o \kappa_2} \left[\dot{\Psi}_{s_1}^d + R_s \kappa_1 \Psi_{s_1}^d - \alpha \Psi_{r_2}^d e - R_s \kappa_1 \eta_{s_1} + \kappa_{s_1} \eta_{s_1} - V_{s_1} \right] \quad (3.32)$$

where $\kappa_{s_1} \in \mathbb{R}^+$ is a control gain. The auxiliary control input, $\omega_s(t)$, is designed to be

$$\omega_s = \frac{1}{\Psi_{s_1}^d} \left[R_s \kappa_2 \Psi_{r_2}^d - \alpha \Psi_{r_1}^d e + R_s \kappa_1 \eta_{s_2} - \kappa_{s_2} \eta_{s_2} + V_{s_2} \right] \quad (3.33)$$

where $\kappa_{s_2} \in \mathbb{R}^+$ is a control gain.

The control voltage, $V_r(t)$ is designed as follows

$$\begin{aligned}
V_{r_1} = & \frac{\ddot{\Psi}_{s_1}^d}{R_o \kappa_2} + \Theta_1 \dot{\Psi}_{s_1}^d - \Theta_2 \Psi_{s_1}^d + \Theta_3 \Psi_{r_1}^d + \Theta_4 \Psi_{r_2}^d + (\Theta_5 - \Theta_6 e + \Theta_7 e^2) e \\
& + (\Theta_8 - \Theta_9 \Psi_{r_2}^d e) \eta_{s_1} - (\Theta_{10} + \Theta_{11} e) \eta_{s_2} \\
& + (\Theta_{12} - \Theta_9 e) \eta_{s_2} \eta_{r_1} + \Theta_{13} \eta_{r_1} + \frac{(R_s \kappa_1 - \kappa_{s_1})}{R_s \kappa_2} V_{L_1}
\end{aligned} \tag{3.34}$$

$$\begin{aligned}
V_{r_2} = & \Omega_1 - \Omega_2 \hat{f}_s - \Omega_3 e + \alpha e \eta_{s_1} + \Omega_4 \Psi_{r_2}^d \eta_{s_1} + \Omega_5 \eta_{s_2} + \frac{\alpha^2 \Psi_{s_1}^d \Psi_{r_2}^d}{R_s \kappa_2 M_m} \eta_{r_1} \\
& - (\Omega_6 - \Omega_7 \eta_{s_1}) e \eta_{r_1} - \frac{\alpha^2 \Psi_{r_2}^d}{R_s \kappa_2 M_m} \eta_{s_1} \eta_{r_1} + \Omega_8 \eta_{s_2} \eta_{r_1} - \Omega_8 \eta_{s_1} \eta_{r_2} + \Omega_9 \eta_{r_2} - \Omega_{10} e^2
\end{aligned} \tag{3.35}$$

where the terms $\Theta_i(t), \Omega_j(t)$, $i = 1, \dots, 13$ and $j = 1, \dots, 10$, are explicitly defined in

Appendix D.

Analysis of Tracking Error Systems

Theorem 3.1: *Given the error system in (3.28)-(3.30) and the designed terms in (3.31)-(3.35), the tracking error signals given in (3.23)-(3.25) are globally uniformly ultimately bounded (GUUB) and all signals remain bounded under closed-loop operation.*

Proof: A non-negative function, denoted by $V(t) \in \mathbb{R}$, is defined as

$$V = 0.5 M_m e^2 + 0.5 \eta_s^T \eta_s + 0.5 \eta_r^T \eta_r. \tag{3.36}$$

which can be re-written as

$$V = 0.5 z^T \text{diag}\{M_m, 1, 1, 1, 1\} z \tag{3.37}$$

and can thus be bounded using the Raleigh inequality as

$$\lambda_{\min} \|z\|^2 \leq V \leq \lambda_{\max} \|z\|^2 \quad (3.38)$$

where $z(t) \in \mathbb{R}^5$ is defined as $z = \begin{bmatrix} e & \eta_s^T & \eta_r^T \end{bmatrix}^T$, $\lambda_{\min} = 0.5 \min(M_m, 1)$ and

$$\lambda_{\max} = 0.5 \max(M_m, 1).$$

Taking the time derivative of (3.36) results in

$$\dot{V} = eM_m \dot{e} + \begin{bmatrix} \eta_{s_1} & \eta_{s_2} \end{bmatrix} \begin{bmatrix} \dot{\eta}_{s_1} \\ \dot{\eta}_{s_2} \end{bmatrix} + \begin{bmatrix} \eta_{r_1} & \eta_{r_2} \end{bmatrix} \begin{bmatrix} \dot{\eta}_{r_1} \\ \dot{\eta}_{r_2} \end{bmatrix}. \quad (3.39)$$

After substituting (3.28)-(3.30) into (3.39), $\dot{V}(t)$ can be expressed as

$$\begin{aligned} \dot{V} = & e \left[M_m \dot{\omega}_d + f - \tau_d - \alpha \Psi_{s_1}^d \eta_{r_2} + \alpha \Psi_{r_1}^d \eta_{s_2} - \alpha \Psi_{r_2}^d \eta_{s_1} - \alpha \eta_{s_2} \eta_{r_1} + \alpha \eta_{s_1} \eta_{r_2} \right] \\ & + \begin{bmatrix} \eta_{s_1} \\ \eta_{s_2} \end{bmatrix}^T \left\{ \begin{bmatrix} \Psi_{s_1}^d \\ 0 \end{bmatrix} + R_s \kappa_1 \begin{bmatrix} \Psi_{s_1}^d \\ 0 \end{bmatrix} - R_s \kappa_1 \begin{bmatrix} \eta_{s_1} \\ \eta_{s_2} \end{bmatrix} \right. \\ & + R_s \kappa_2 \begin{bmatrix} \eta_{r_1} \\ \eta_{r_2} \end{bmatrix} - R_s \kappa_2 \begin{bmatrix} \Psi_{r_1}^d \\ \Psi_{r_2}^d \end{bmatrix} + \begin{bmatrix} 0 \\ \Psi_{s_1}^d \end{bmatrix} \omega_s + \begin{bmatrix} \eta_{s_2} \\ -\eta_{s_1} \end{bmatrix} \omega_s - V_s \left. \vphantom{\begin{bmatrix} \eta_{s_1} \\ \eta_{s_2} \end{bmatrix}^T} \right\} \\ & + \begin{bmatrix} \eta_{r_1} & \eta_{r_2} \end{bmatrix} \left\{ \begin{bmatrix} \dot{\Psi}_{r_1}^d \\ \dot{\Psi}_{r_2}^d \end{bmatrix} + R_r \kappa_2 \begin{bmatrix} \eta_{s_1} \\ \eta_{s_2} \end{bmatrix} - R_r \kappa_2 \begin{bmatrix} \Psi_{s_1}^d \\ 0 \end{bmatrix} \right. \\ & + R_r \kappa_1 \left(\begin{bmatrix} \Psi_{r_1}^d \\ \Psi_{r_2}^d \end{bmatrix} - \begin{bmatrix} \eta_{r_1} \\ \eta_{r_2} \end{bmatrix} \right) - \begin{bmatrix} V_{r_1} \\ V_{r_2} \end{bmatrix} + \begin{bmatrix} -\Psi_{r_2}^d \\ \Psi_{r_1}^d \end{bmatrix} \omega_s \left. \vphantom{\begin{bmatrix} \eta_{r_1} & \eta_{r_2} \end{bmatrix}} \right\}. \end{aligned} \quad (3.40)$$

Substituting (3.31)-(3.35) as well as the mathematical derivatives of $\Psi_{r_1}^d(t)$ and

$\Psi_{r_2}^d(t)$, results in

$$\begin{aligned}
\dot{V} = & ef + e\hat{f}_s - Ke^2 - \kappa_{s_1}\eta_{s_1}^2 - \kappa_{s_2}\eta_{s_2}^2 - \kappa_{r_1}\eta_{r_1}^2 - \kappa_{r_2}\eta_{r_2}^2 \\
& - \frac{\rho^2(\omega)e^2}{\varepsilon} - \frac{\rho_1^2(\cdot)\eta_{r_1}^2}{\varepsilon_1} - \frac{\rho_2^2(\cdot)\eta_{r_2}^2}{\varepsilon_2} \\
& + \frac{\left(\frac{2Ke + M_m\dot{\omega}_d + \hat{f}_s}{\varepsilon} - \frac{2\rho(\omega)e(\partial\rho(\omega)e - \rho(\omega))}{\varepsilon} \right)}{R_o\kappa_2M_m\Psi_{s_1}^d} f(\cdot)\eta_{r_1} \\
& - \left(K - \frac{\rho(\omega)(2\partial\rho(\omega)e - \rho(\omega))}{\varepsilon} \right) \frac{f(\cdot)\eta_{r_2}}{\alpha M_m\Psi_{s_1}^d}
\end{aligned} \tag{3.41}$$

where $\partial\rho(\omega)$ denotes the partial derivative of $\rho(\omega)$ with respect to ω .

Remark 3.7: The functions $\rho_1(\cdot)$ and $\rho_2(\cdot)$ are designed in Appendix E such that

$$\rho_1(\cdot) \geq \frac{\left| \left(\frac{2Ke + M_m\dot{\omega}_d + \hat{f}_s}{\varepsilon} - \frac{2\rho(\omega)e(\partial\rho(\omega)e - \rho(\omega))}{\varepsilon} \right) f \right|}{|R_o\kappa_2M_m\Psi_{s_1}^d|} \tag{3.42}$$

$$\rho_2(\cdot) \geq \left| \left(K - \frac{2\rho(\omega)\partial\rho(\omega)}{\varepsilon} + \frac{\rho^2(\omega)}{\varepsilon} \right) \frac{f}{\alpha M_m\Psi_{s_1}^d} \right| \tag{3.43}$$

From (3.41), using Remarks 3.2, 3.6 and 3.7, the function $\dot{V}(t)$ can be upper bounded as

follows

$$\begin{aligned}
\dot{V} \leq & -K_1e^2 - \kappa_{s_1}\eta_{s_1}^2 - \kappa_{s_2}\eta_{s_2}^2 - \kappa_{r_1}\eta_{r_1}^2 - \kappa_{r_2}\eta_{r_2}^2 + \{\rho_s|e| - K_2e^2\} \\
& + \rho(\cdot)|e| \left[1 - \frac{\rho(\cdot)|e|}{\varepsilon} \right] + \rho_1(\cdot)|\eta_{r_1}| \left[1 - \frac{\rho_1(\cdot)|\eta_{r_1}|}{\varepsilon_1} \right] + \rho_2(\cdot)|\eta_{r_2}| \left[1 - \frac{\rho_2(\cdot)|\eta_{r_2}|}{\varepsilon_2} \right].
\end{aligned} \tag{3.44}$$

where the control gain, K , introduced in (3.31) is designed as $K = K_1 + K_2$ with $K_1, K_2 \in \mathbb{R}^+$. Applying the nonlinear damping argument [5] to the curly bracketed terms on the right hand side of (3.44) results in the following upper bound for $\dot{V}(t)$

$$\dot{V} \leq -\gamma \|z\|^2 + \bar{\varepsilon} \quad (3.45)$$

where $\bar{\varepsilon}, \gamma \in \mathbb{R}^+$ and are defined as $\bar{\varepsilon} = \varepsilon + \varepsilon_1 + \varepsilon_2 + \frac{\rho_s^2}{K_2}$ and

$$\gamma = \min(K_1, \kappa_{s_1}, \kappa_{s_2}, \kappa_{r_1}, \kappa_{r_2}).$$

From (3.38) and (3.45), the following relationship is obtained.

$$\dot{V} \leq -\frac{\gamma V}{\lambda_{\max}} + \bar{\varepsilon}. \quad (3.46)$$

From (3.38) and (3.46), the error signal $\|z(t)\|$ can be upper bounded as

$$\|z(t)\| \leq \sqrt{\beta_0 \exp(-\beta_1 t) + \beta_2 [1 - \exp(-\beta_1 t)]} \quad (3.47)$$

where $\beta_0 \triangleq \frac{\lambda_{\max}}{\lambda_{\min}} \|z(t_0)\|^2$, $\beta_1 \triangleq \frac{\gamma}{\lambda_{\max}}$, and $\beta_2 \triangleq \frac{\lambda_{\max} \bar{\varepsilon}}{\lambda_{\min} \gamma}$.

From (3.47), it can be shown that $e(t), \eta_s(t), \eta_r(t) \in \mathcal{L}_\infty$. Since $e(t) \in \mathcal{L}_\infty$, (3.23) can be used along with Remark 3.3, to show that $\omega(t) \in \mathcal{L}_\infty$. After utilizing the fact that $\omega(t) \in \mathcal{L}_\infty$, from Assumption 6, it is apparent that $f(\cdot) \in \mathcal{L}_\infty$. After using Remarks 3.3 and 3.6 and the fact that $e(t) \in \mathcal{L}_\infty$, along with (3.31), it can be shown that $\tau_d(t) \in \mathcal{L}_\infty$.

Remark 3.5 can be used along with the facts that $\tau_d(t), \Psi_{s_1}^d(t) \in \mathcal{L}_\infty$ to show

that $\Psi_{r_2}^d(t) \in \mathcal{L}_\infty$. The expression in (3.32) can be used along with the above boundedness statements to show that $\Psi_{r_1}^d(t) \in \mathcal{L}_\infty$. Since all the signals on the right-hand-side of (3.28) are bounded then it can be concluded that $\dot{e}(t)$ is also bounded. From the time derivative of (3.23), it is easy to see that $\dot{\omega}(t)$ is bounded; thus from Assumption 6, it is clear that $\dot{f}(\cdot)$ is bounded. The mechanical subsystem dynamics in (3.5) can be utilized to show that $\tau_{em}(t)$ is bounded. Above boundedness statements can be utilized along with (3.24), (3.25) and (3.33) to show that $\Psi_s(t), \Psi_r(t), \omega_s(t) \in \mathcal{L}_\infty$. Since $\omega(t)$ and $\dot{\omega}(t)$ are bounded, it is clear that $\dot{\rho}(\cdot) \in \mathcal{L}_\infty$. Above boundedness statements can be used along with Assumption 4, Remarks 3.3, 3.4 and 3.6 to prove that all the terms in Appendices E and F are bounded; thus from (3.34) and (3.35), it can be concluded that $V_{r_1}(t), V_{r_2}(t) \in \mathcal{L}_\infty$. After utilizing the fact that $\dot{\Psi}_{s_1}^d(t) \in \mathcal{L}_\infty$ along with the above boundedness statements, from (3.29), it is easy to see that $\dot{\eta}_s(t) \in \mathcal{L}_\infty$. The time derivatives of (3.31) and (3.32) can be utilized to show that $\dot{\tau}_d(t)$ and $\dot{\Psi}_{r_1}^d(t)$ are bounded. $\dot{\Psi}_{r_2}^d(t)$ can be shown to be bounded from the time derivative of the expression in Remark 3.5. From (3.30), it can be concluded that $\dot{\eta}_{r_1}(t), \dot{\eta}_{r_2}(t) \in \mathcal{L}_\infty$. The fact that $\dot{\eta}_s(t), \dot{\eta}_r(t) \in \mathcal{L}_\infty$ can be used along with the time derivatives of (3.24) and (3.25) to show that $\dot{\Psi}_s(t)$ and $\dot{\Psi}_r(t)$ are bounded; thus from the time derivative of (3.18), it is clear that $\dot{\tau}_{em}(t)$ is bounded. After taking the time derivative of (3.5), it can be concluded

that $\ddot{\omega}(t) \in \mathcal{L}_\infty$; thus from the second time derivative of (3.23), it is clear that $\ddot{e}(t) \in \mathcal{L}_\infty$ where Remark 3.3 is utilized. From Assumption 6, it may be concluded that $\ddot{f}(\cdot) \in \mathcal{L}_\infty$. The application of standard signal chasing arguments permits the conclusion that all signals in the closed loop system remain bounded.

Nonlinearity Observer Design

The control objective is to maximize the aerodynamic rotor power captured by a variable speed wind turbine with structurally uncertain system nonlinearities by controlling the rotor speed, $\omega(t)$. The existence of uncertain system nonlinearities motivates the design of a system nonlinearity observer, denoted by $\hat{f}(\cdot) \in \mathbb{R}$, to estimate $f(\cdot)$. This estimate is developed for two reasons:

1. $\hat{f}(\cdot)$ is used as a feed-forward term in the control design through $\hat{f}_s(\cdot)$.
2. Since $P_{\text{aero}}(t)$ is unmeasurable, an estimate of the captured power, denoted by $\hat{P}_{\text{aero}}(t) \in \mathbb{R}$, is designed where $\hat{P}_{\text{aero}}(t) = -\hat{f}(t)\omega(t)$, and is used in the online planning of $\omega_d(t)$.

Observer Error Systems

The main objective of the observer is to estimate the system nonlinearities $f(\cdot)$ such that $\hat{f}(\cdot) \rightarrow f(\cdot)$ as $t \rightarrow \infty$. To facilitate the observer design, the following system model is developed

$$M_m \dot{\hat{\omega}} = \tau_{em} - \hat{f} \quad (3.48)$$

where $\hat{\omega}(t) \in \mathbb{R}$ denotes the estimated rotor speed.

The rotor speed and nonlinearity observation errors, $\tilde{\omega}(t), \tilde{f}(t) \in \mathbb{R}$ are defined as

$$\tilde{\omega} \triangleq \hat{\omega} - \omega, \quad \tilde{f} \triangleq \hat{f} - f. \quad (3.49)$$

In addition, the filtered rotor speed observation error, denoted by $r(t) \in \mathbb{R}$, is defined to facilitate the subsequent design and analysis as

$$r \triangleq \dot{\tilde{\omega}} + k\tilde{\omega} \quad (3.50)$$

where $k \in \mathbb{R}^+$ is a control gain. After taking the time derivative of (3.50) and pre-multiplying by M_m , it can be seen that

$$M_m \dot{r} = -\dot{\tilde{f}} + \dot{f} + \Phi - \tilde{\omega} \quad (3.51)$$

where $\Phi(t) \in \mathbb{R}$ is defined as $\Phi = kM_m \dot{\tilde{\omega}} + \tilde{\omega}$.

Remark 3.8: *The mean value theorem can be utilized to upper bound $\Phi(t)$ such that*

$|\Phi(t)| \leq \rho_N \|X\|$ where $X(t) = [\tilde{\omega}(t), r(t)]^T \in \mathbb{R}^2$ and $\rho_N \in \mathbb{R}^+$ is a bounding constant [6].

Observer Design

Based on the structure of (3.51), as well as the subsequent stability analysis, a continuous estimator law is proposed to achieve the stated estimator objectives with

$$\dot{\hat{f}} = (k_f + k)r + \rho_0 \operatorname{sgn}(\tilde{\omega}) \quad (3.52)$$

where $k_f, \rho_0 \in \mathbb{R}^+$ are control gains and $\operatorname{sgn}(\cdot) \in \mathbb{R}$ is the standard signum function.

Analysis of Observer Error Systems

Before presenting the stability analysis, the following lemma will be introduced and later invoked.

Lemma 3.1: *Let the auxiliary function $L(t) \in \mathbb{R}$ be defined as*

$$L \triangleq r(\dot{\hat{f}} - \rho_0 \operatorname{sgn}(\tilde{\omega})) \quad (3.53)$$

If the control gain ρ_0 is selected to satisfy the sufficient condition

$\rho_0 > \left| \dot{\hat{f}}(\cdot) \right| + \frac{\left| \ddot{\hat{f}}(\cdot) \right|}{k}$, then $\int_{t_0}^t L(v) dv \leq \zeta$ where $\zeta \in \mathbb{R}^+$ is defined as

$$\zeta \triangleq \rho_0 \left| \tilde{\omega}(t_0) \right| - \tilde{\omega}(t_0) \dot{\hat{f}}(t_0). \quad (3.54)$$

Proof: See Appendix F.

Theorem 2: The observer design in (3.52) ensures that asymptotic tracking is obtained in the sense that $\tilde{\omega}(t), \dot{\tilde{\omega}}(t), r(t) \rightarrow 0$ and $\hat{f}(t) \rightarrow f(t)$ as $t \rightarrow \infty$.

Proof: Define an auxiliary function $P(t) \in \mathbb{R}$ as

$$P = \zeta - \int_{t_0}^t L(v) dv \quad (3.55)$$

where $\zeta, L(t)$ have been defined in Lemma 3.1. Based on the non-negativity of

$P(t)$ (see proof of Lemma 3.1), we define a nonnegative function $V_o(t) \in \mathbb{R}$ as follows

$$V_o(t) = \frac{1}{2} \tilde{\omega}^2 + \frac{1}{2} M_m r^2 + P. \quad (3.56)$$

After taking the time derivative of (3.56) and utilizing (3.51), (3.53), and the time derivative of (3.55), we can conveniently rearrange terms to obtain the following expression

$$\dot{V}_o = -k \tilde{\omega}^2 - r \dot{f} + r \Phi + r \rho_0 \operatorname{sgn}(\tilde{\omega}). \quad (3.57)$$

After substituting (3.52) and utilizing Remark 3.8, simple algebraic manipulations can be used to obtain the following upper bound for $\dot{V}_o(t)$

$$\dot{V}_o \leq -k \|X\|^2 + \left[|r| \rho_N \|X\| - k_f |r|^2 \right]. \quad (3.58)$$

Applying the nonlinear damping argument [5] to the bracketed term in (3.58) results in the following upper bound for $\dot{V}_o(t)$

$$\dot{V}_o \leq - \left[k - \frac{\rho_N^2}{k_f} \right] \|X\|^2. \quad (3.59)$$

From (2.32), it is possible to state that

$$\dot{V}_o \leq -\zeta \|X\|^2 \text{ for } k_f > \frac{\rho_N^2}{k} \quad (3.60)$$

where $\zeta \in \mathbb{R}^+$ is a constant. From (3.60) and the analysis in this section, we can conclude that $X(t) \in \mathcal{L}_\infty$. From the definition of $X(t)$, it can be inferred that

$\tilde{\omega}(t), \dot{\tilde{\omega}}(t), r(t) \in \mathcal{L}_\infty$. From (3.52), it is clear that $\dot{\hat{f}}(\cdot) \in \mathcal{L}_\infty$. Using standard signal chasing arguments, it can be shown that all the signals in the closed-loop system remain bounded. In particular, from (3.51), it can be seen that $\dot{r}(t) \in \mathcal{L}_\infty$; thus

$\dot{X}(t) \in \mathcal{L}_\infty$. After employing a corollary to Barbalat's Lemma [6], it is easy to show that

$\|X(t)\| \rightarrow 0$ as $t \rightarrow \infty$. From the definition of $X(t)$, it can be concluded that

$\tilde{\omega}(t), r(t) \rightarrow 0$ as $t \rightarrow \infty$. From (3.50), it is easy to see that $\dot{\tilde{\omega}}(t) \rightarrow 0$ as $t \rightarrow \infty$.

From (3.48), the following relationship can be obtained

$$M_m \dot{\tilde{\omega}} = f - \hat{f} = -\tilde{f}. \quad (3.61)$$

From (3.61), it is clear that $\dot{\tilde{\omega}}(t) \rightarrow 0$ implies that $|\tilde{f}(t)| \rightarrow 0$ thus $\hat{f}(t) \rightarrow f(t)$

so $\hat{P}_{\text{aero}}(t) \rightarrow P_{\text{aero}}(t)$ as $t \rightarrow \infty$.

Trajectory Generator

In Remark 3.3, it was assumed that a desired trajectory $\omega_d(t)$ can be designed such that $\omega_d(t), \dot{\omega}_d(t)$ and $\ddot{\omega}_d(t)$ are bounded and $\omega_d(t) \rightarrow \omega^*$, where ω^* is the unknown rotor speed that maximizes the aerodynamic rotor power, $P_{\text{aero}}(t)$, for a particular wind speed, $v(t)$, and blade pitch angle, β . As stated in Remark 3.1, $P_{\text{aero}}(t)$

is unmeasurable, therefore the estimated captured power, $\hat{P}_{\text{aero}}(t)$, is used as the cost function to be optimized. The Successive Quadratic Estimator (SQE) is selected as the optimum seeking algorithm. The advantage of this algorithm over conventional methods, such as the Golden Section Search and Simplex, is that no initial cost function values or bounds on the functional values are required. The estimator approximates the unimodal cost function, $\hat{P}_{\text{aero}}(\hat{\omega}(t))$, as a quadratic function over a local bound and successively uses this property to predict the location of ω^* , the optimum rotor speed [7].

To ensure that $\omega_d(t)$, $\dot{\omega}_d(t)$ and $\ddot{\omega}_d(t)$ are bounded, a filter based form of the SQE is used, wherein at each iteration (new guess), $\omega_d[n]$ is passed through a set of third order stable and proper low pass filters to generate continuous bounded signals for $\omega_d(t)$, $\dot{\omega}_d(t)$ and $\ddot{\omega}_d(t)$. The following filters are used in this study:

$$\omega_d(t) = \frac{\zeta_1}{s^3 + \zeta_2 s^2 + \zeta_3 s + \zeta_4} \omega_d[n] \quad (3.62)$$

$$\dot{\omega}_d(t) = \frac{\zeta_1 s}{s^3 + \zeta_2 s^2 + \zeta_3 s + \zeta_4} \omega_d[n] \quad (3.63)$$

$$\ddot{\omega}_d(t) = \frac{\zeta_1 s^2}{s^3 + \zeta_2 s^2 + \zeta_3 s + \zeta_4} \omega_d[n] \quad (3.64)$$

where $\zeta_1, \zeta_2, \zeta_3, \zeta_4 \in \mathbb{R}^+$ are filter constants. The optimization algorithm waits until certain error thresholds are met before making the next guess (*i.e.*, if

$|\omega_d(t) - \omega_d[n]| \leq \bar{e}_1, |\tilde{f}(\cdot)| \leq \bar{e}_2$ and $|\omega(t) - \omega_d(t)| \leq \bar{e}_3$ then $n = n + 1$ where $\bar{e}_1, \bar{e}_2, \bar{e}_3 \in \mathbb{R}^+$ are threshold constants and $n \in \mathbb{Z}^+$).

Simulation Results

A numerical case study is presented in this section to demonstrate the performance of the control strategy and the numerical-based optimum seeking reference trajectory generator using MATLAB/Simulink. The plant model in (3.5) was assumed to correspond to a small wind turbine, possessing the following system nonlinearity

$$f(\cdot) = -\frac{1}{2} \rho_a A \frac{C_p(\lambda)}{\omega} v^3. \quad (3.65)$$

For simulation purposes, a 350W EXTRACTOR wind turbine and a ½ hp two-pole induction generator were selected. The simulation parameters are listed in Appendix G. The resulting rotor speed tracking error $e(t)$ and flux tracking errors

$\eta_{s_1}(t), \eta_{s_2}(t), \eta_{r_1}(t)$ and $\eta_{r_2}(t)$ are shown in Figs. 3.1, 3.2, 3.3, 3.4 and 3.5, respectively.

From these figures, it can be seen that globally uniformly bounded tracking errors have been achieved under the proposed control strategy. The voltage control inputs $V_{r_1}(t)$ and $V_{r_2}(t)$ are shown in Figs. 3.6 and 3.7, respectively. The power coefficient function,

$C_p(\lambda)$, for the wind turbine, illustrated in Fig. 3.8, is an example curve obtained using blade-element momentum theory [8]. It may be observed that $C_p^{\max} = 0.4405$ occurs

when $\lambda^* = 3.5$ which corresponds to $\omega^* = 5.296$. The actual power efficiency measure,

$C_p(t)$, shown in Fig. 3.9, shows that $C_p(t) \rightarrow 0.4401$ as $\omega(t) \rightarrow 5.3569$, as illustrated in Fig. 3.10. Additionally, the copper loss, $P_{loss}(t)$, desired stator flux, $\Psi_{s_1}^d(t)$ and estimator error $\tilde{f}(t)$ are shown in Figs. 3.11, 3.12 and 3.13, respectively. Overall, the simulation results demonstrate that the proposed control strategy performed satisfactorily and shows a robust response to structural uncertainties.

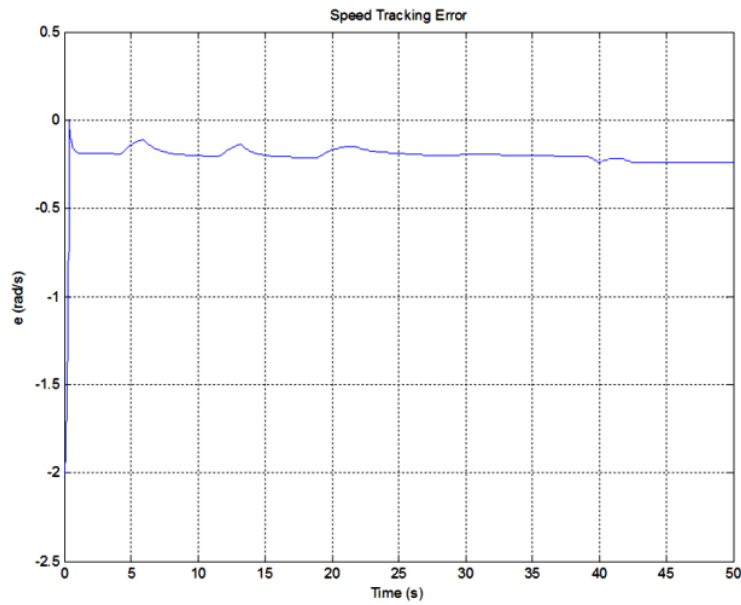


Figure 3.1: Rotor speed tracking error $e(t)$

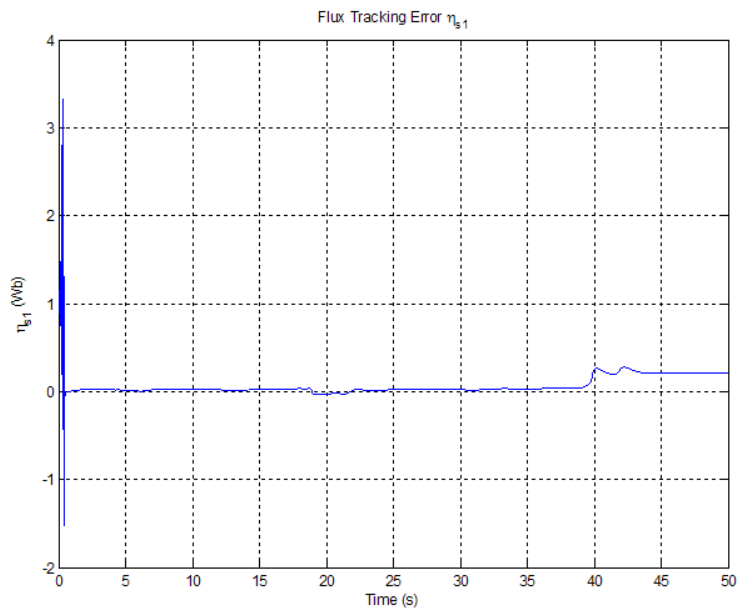


Figure 3.2: Stator flux tracking error $\eta_{s_1}(t)$

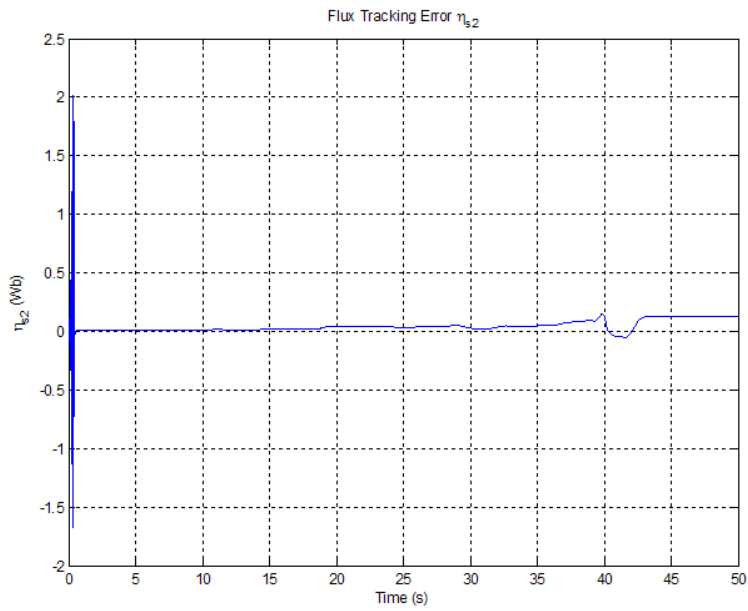


Figure 3.3: Stator flux tracking error $\eta_{s_2}(t)$

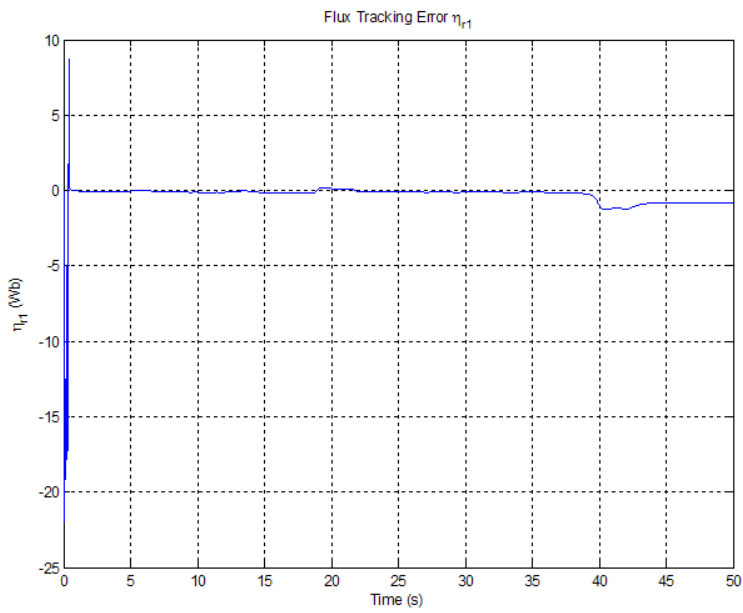


Figure 3.4: Rotor flux tracking error $\eta_{r_1}(t)$

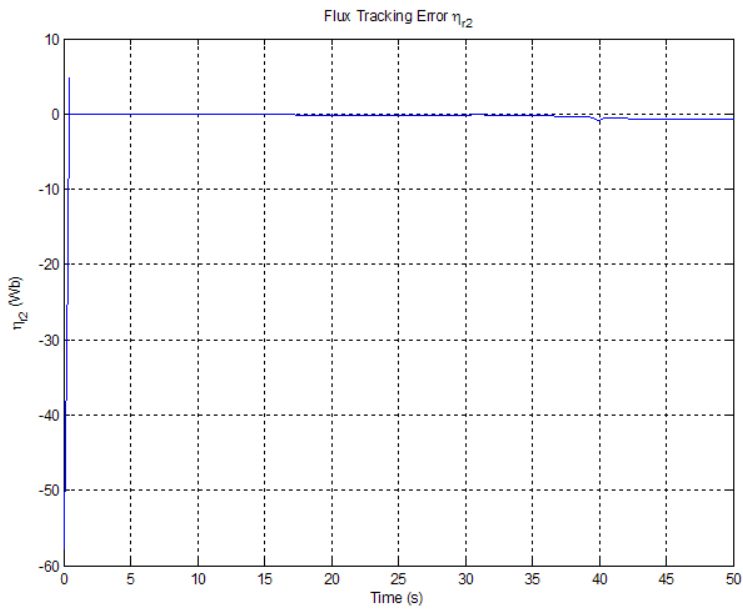


Figure 3.5: Rotor flux tracking error $\eta_{r_2}(t)$

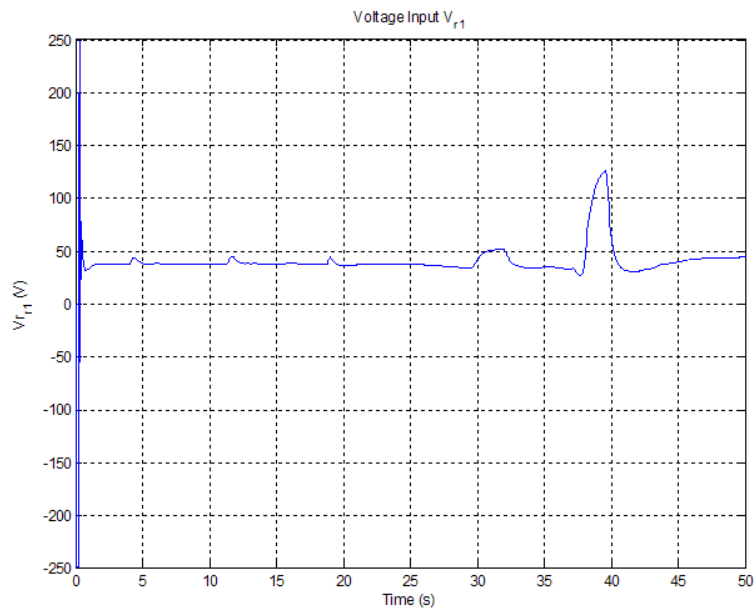


Figure 3.6: Voltage control input $V_{r_1}(t)$

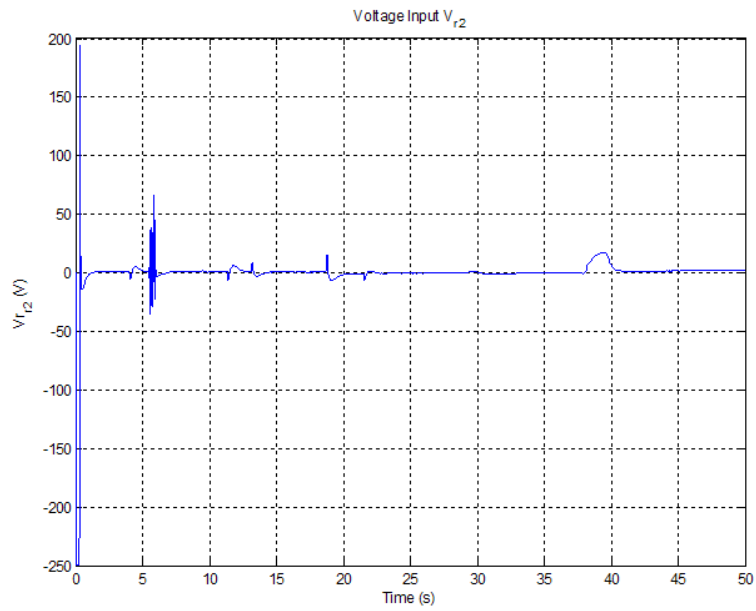


Figure 3.7: Voltage control input $V_{r_2}(t)$

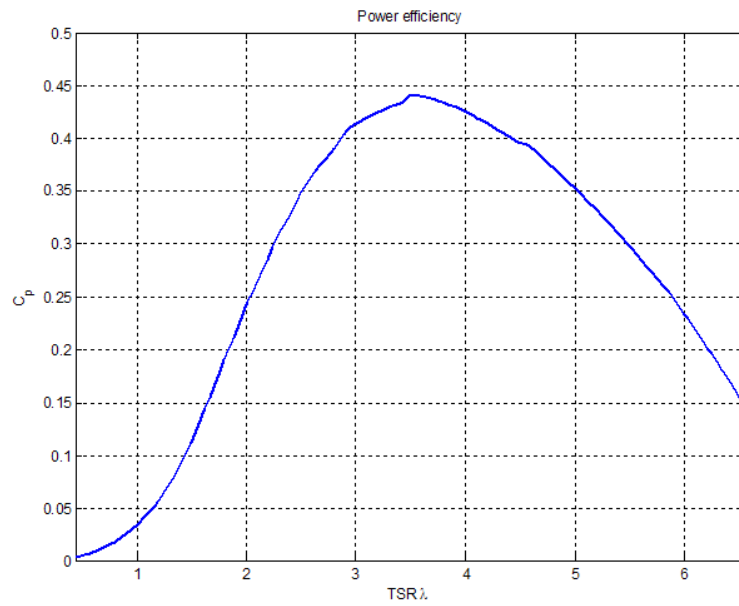


Figure 3.8: Power efficiency curve of the simulated wind turbine

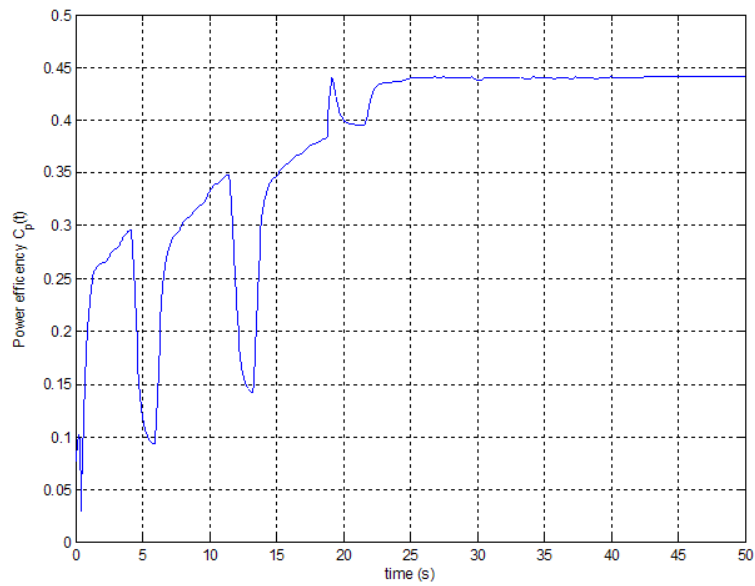


Figure 3.9: Rotor power coefficient $C_p(t)$ resulting from optimization algorithm

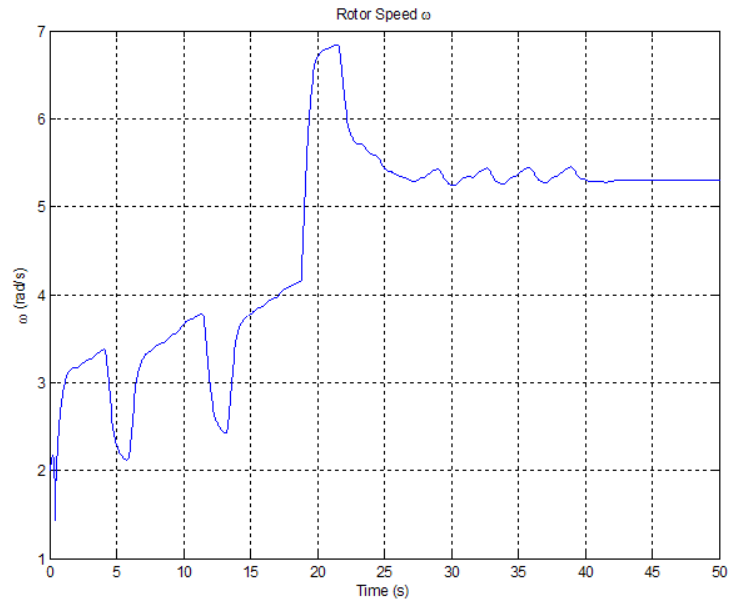


Figure 3.10: Rotor Speed $\omega(t)$

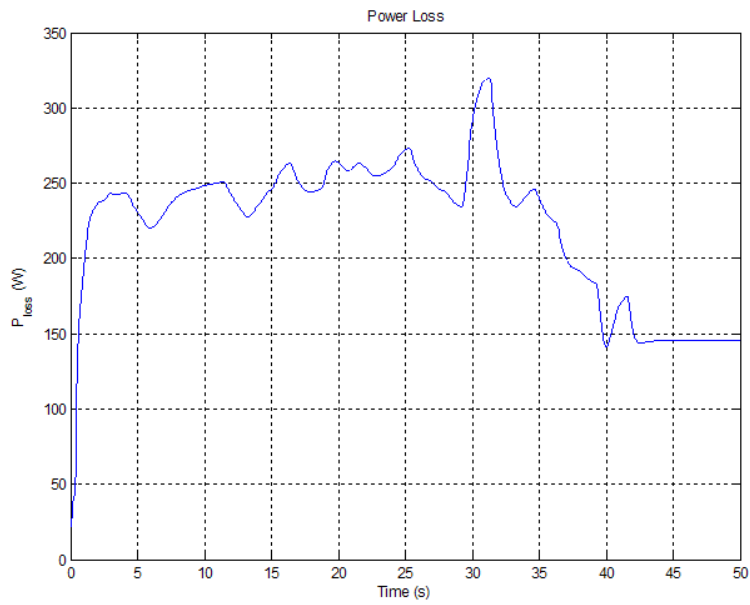


Figure 3.11: Copper losses $P_{loss}(t)$

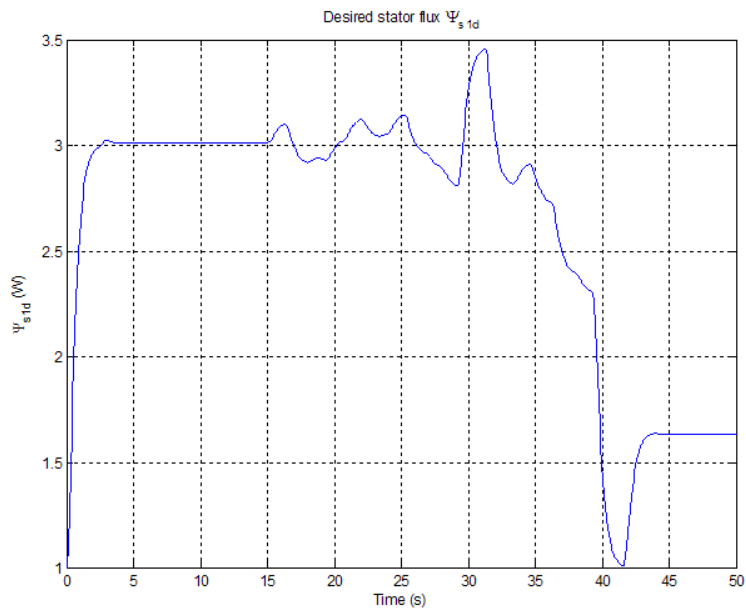


Figure 3.12: Desired Stator flux $\Psi_{s_1}^d(t)$

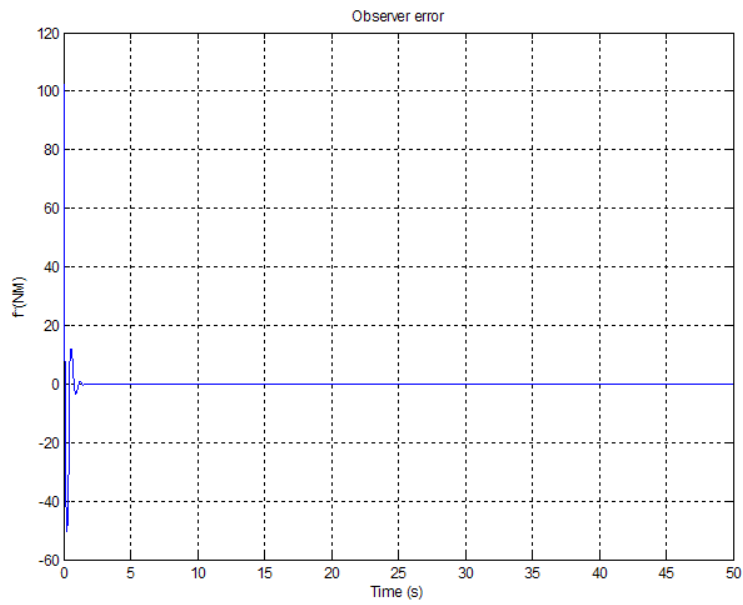


Figure 3.13: Nonlinearity observation error $\tilde{f}(t)$

References

- [1] K. Johnson, L. Fingersh, M. Balas, and L. Pao, "Methods for increasing region 2 power capture on a variable-speed wind turbine", *J. Solar Energy Eng.*, vol. 126, no. 4, pp. 1092-1100, 2004.
- [2] P. Krause, *Analysis of Electrical Machinery*. New York: McGraw Hill, 1986.
- [3] R. Marino, S. Peresada, and P. Valigi, "Adaptive input-output linearizing control of induction motors," *IEEE Trans. Automat. Contr.*, vol. 38, no. 2, pp. 208-221, Feb. 1993.
- [4] R. Marino, S. Peresada and P. Tomei, "Global adaptive output feedback control of induction motors with uncertain rotor resistance," *IEEE Trans. Automat. Contr.*, vol. 44, pp. 967-983, May 1999.
- [5] P. Kokotovic, "The joy of feedback: nonlinear and adaptive," *IEEE Control Syst. Mag.*, vol. 12, no. 3, pp. 7-17, Jun. 1992.
- [6] J. Slotine and W. Li, *Applied Nonlinear Control*, Englewood Cliffs, NJ: Prentice Hall, 1991.
- [7] G. Reklaitis, A. Ravindran, and K. Ragsdell, *Engineering Optimization*, Hoboken, NJ: John Wiley & Sons, 1983, pp. 41-130.
- [8] NWTC Design Codes (WT_Perf by Marshall Buhl), <http://wind.nrel.gov/designcodes/simulators/wtperf/>, Aug. 1, 2007.

CHAPTER FOUR

BACKSTEPPING PWM CONTROL FOR MAXIMUM POWER TRACKING IN PHOTOVOLTAIC ARRAY SYSTEMS

In this chapter, a control strategy is developed to maximize the power of a solar generating system charging a constant-voltage battery via a DC-DC boost converter. In the first section, the dynamic model of the solar generating system is described. Next, a backstepping array voltage tracking controller is designed along with the corresponding closed-loop error system. The Lyapunov-based stability analysis of the closed-loop error system is then discussed in next section. The desired array voltage trajectory is designed/generated in the following section. Finally, numerical simulation results are presented to illustrate the performance of the control strategy.

Problem Statement

The control objective is to determine the maximum power operating point (MPOP) by tracking a desired array voltage which can be achieved by modulating the pulse width of the switch control signal (increasing or decreasing the duty ratio of the switching converter). The desired array voltage is designed online using a filtered incremental conductance MPP tracking algorithm.

Photovoltaic Array System Dynamics

The solar generation model consists of a PV array module, dc-to-dc boost converter and a battery as shown in Fig. 4.1. The converter transfers power from the PV

array terminals to the battery bank, indirectly controlling the voltage of the PV array panel, $v_{pv}(t)$ and thus the array power generation.

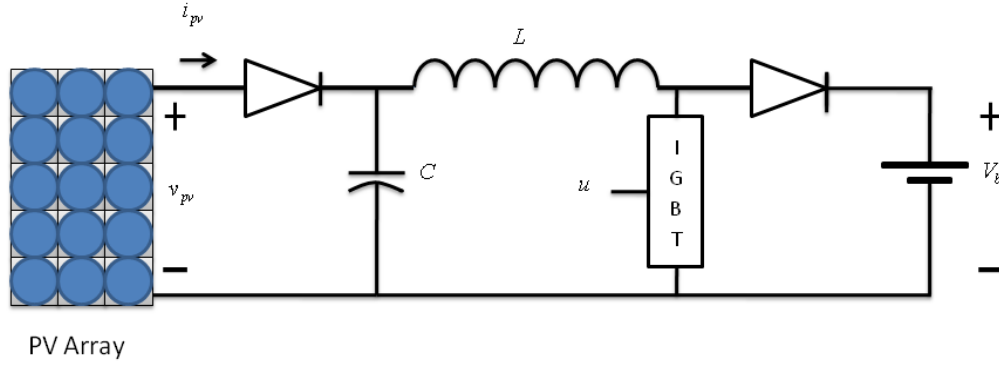


Figure 4.1: The system structure of the photovoltaic array system

The dynamic model of the solar generation system can be expressed by an instantaneous switched model as follows:

$$C\dot{v}_{pv} = i_{pv} - i_L \quad (4.1)$$

$$L\dot{i}_L = v_{pv} - (1-u)V_b \quad (4.2)$$

where L and $i_L(t)$ represents the dc-to-dc converter storage inductance and the current across it; $V_b \in \mathbb{R}$ is the voltage of the storage battery and $u(t) \in \mathbb{R}$ is the switched control signal that can only take the discrete values 0 (switch open) and 1 (switch closed). Using the state averaging method [1], the switched model can be redefined by the average PWM model as follows:

$$C\dot{V}_{pv} = I_{pv} - I_L \quad (4.3)$$

$$L\dot{I}_L = V_{pv} - D'V_b \quad (4.4)$$

where $V_{pv}(t) \in \mathbb{R}$ and $I_{pv}(t) \in \mathbb{R}$ are the average states of the output voltage and current of the solar cell; $I_L(t) \in \mathbb{R}$ is the average state of the inductor current; $D'(t) \in \mathbb{R}$ is the limited duty ratio function of the off-state of the switched control signal, $u(t)$.

To facilitate control development, the following model characteristics are assumed:

Assumption 1: $V_{pv}(t)$, $I_{pv}(t)$, $I_L(t)$ and $V_b(t)$ are measurable.

Assumption 2: C and L are known constants.

Assumption 3: V_b is modeled as a constant value due to its slow charge dynamics [2].

Assumption 4: $I_{pv}(t)$ is bounded provided that $V_{pv}(t)$ is bounded.

Assumption 5: $\dot{I}_{pv}(t)$ can be upper bounded by a positive constant such that $|\dot{I}_{pv}| < \mu$

where $\mu \in \mathbb{R}^+$.

Controller Design

The control objective is to maximize the power extracted from a solar generating system, $P_{pv}(t)$ by tracking a developed desired array voltage, $V_d(t) \in \mathbb{R}$, such that $V_{pv}(t) \rightarrow V_d(t)$ as $t \rightarrow \infty$. This is achieved by varying $D'(t)$, the duty ratio of the off-state of the switched control signal.

Remark 4.1: *The desired array voltage, $V_d(t)$, is designed online using a numerical-based extremum-seeking algorithm, as shown in Section IV, to maximize the extracted power $P_{pv}(t)$ such that $V_d(t) \rightarrow V^*$, where V^* is the unknown optimal array voltage, implies that $P_{pv}(t)$ tends to P_{\max} , the maximum power point (MPP). Additionally, $V_d(t)$ is designed to be sufficiently differentiable, that is $V_d(t), \dot{V}_d(t), \ddot{V}_d(t) \in \mathcal{L}_\infty$.*

Error System Development

To quantify the state control objective, tracking errors denoted by $e(t) \in \mathbb{R}$ and $z(t) \in \mathbb{R}$ are defined as follows

$$e = V_d - V_{pv} \quad (4.5)$$

$$z = I_L - I_D \quad (4.6)$$

where $I_D(t) \in \mathbb{R}$ denotes the subsequently designed desired storage inductor current.

From the definition of the tracking errors in (4.5) and (4.6), and the system dynamics in (4.3) and (4.4), an open loop system is developed as follows:

$$C\dot{e} = C\dot{V}_d - I_{pv} + z + I_D \quad (4.7)$$

$$L\dot{z} = V_{pv} - D'V_b - LI_D \quad (4.8)$$

Control Input Design

The control inputs will be designed based on the subsequent stability analysis as well as the structure of the open loop error systems in (4.7) and (4.8).

The designed desired storage inductor current, $I_D(t)$ is designed as

$$I_D = -C\dot{V}_d + I_{pv} - k_e e \quad (4.9)$$

The duty ratio, $D'(t)$ is designed as follows

$$D' = \frac{1}{V_b} \left[V_{pv} + LC\ddot{V}_d + Lk_e \left(\dot{V}_d - \frac{I_{pv}}{C} + \frac{I_L}{C} \right) + e + k_z z + k_1 \operatorname{sgn}(z) \right]. \quad (4.10)$$

where $k_e, k_1, k_z \in \mathbb{R}^+$ are control gains, and $\operatorname{sgn}(\cdot)$ is the standard signum function.

Substituting (4.9) and (4.10) into the open loop error dynamics of (4.7) and (4.8), results in the following closed loop error system

$$C\dot{e} = -k_e e + z \quad (4.11)$$

$$L\dot{z} = -k_z z - e - k_1 \operatorname{sgn}(z) - LI_{pv} \quad (4.12)$$

Stability Analysis

Theorem 1: *Given the closed loop error system in (4.11) and (4.12), the tracking error signals defined in (4.5) and (4.6) are globally asymptotically regulated in the sense that*

$$e(t), z(t) \rightarrow 0 \text{ as } t \rightarrow \infty \quad (4.13)$$

Proof: A non-negative scalar function, denoted by $V(t) \in \mathbb{R}$, is defined as

$$V = \frac{1}{2} C e^2 + \frac{1}{2} L z^2. \quad (4.14)$$

After taking the time derivative of (4.14) and making the appropriate substitutions from (4.11) and (4.12), the following expression is obtained

$$\dot{V} = e[-k_e e + z] + z[-k_z z - e - k_1 \operatorname{sgn}(z) - L\dot{I}_{pv}]. \quad (4.15)$$

$$\dot{V} = -k_e e^2 - k_z z^2 - k_1 |z| - L\dot{I}_{pv} z. \quad (4.16)$$

From (4.16), $\dot{V}(t)$ can be upper bound as follows

$$\dot{V} \leq -k_e e^2 - k_z z^2 - k_1 |z| + L|\dot{I}_{pv}||z|. \quad (4.17)$$

If the control gain k_1 is designed such that $k_1 > L\mu$ then from Assumption 5,

$\dot{V}(t)$ can be upper bound as follows

$$\dot{V} \leq -k_e e^2 - k_z z^2. \quad (4.18)$$

From (4.14) and (4.18), it is straightforward to see that $e(t), z(t) \in \mathcal{L}_\infty$. Since $e(t) \in \mathcal{L}_\infty$, (4.5) can be used along with Remark 4.1 to show that $V_{pv}(t) \in \mathcal{L}_\infty$. Based on the above boundedness statements, (4.9) can be used along with Remark 4.1 and Assumption 4 to show that $I_d(t) \in \mathcal{L}_\infty$. After utilizing the fact that $I_D(t), z(t) \in \mathcal{L}_\infty$, from (4.6), it is clear that $I_L(t) \in \mathcal{L}_\infty$. The expression in (4.10), Remark 4.1 and Assumptions 3 and 4, can be used along with the above boundedness statements to show that $D'(t) \in \mathcal{L}_\infty$. The above boundedness statements can be utilized along with (4.3), (4.4) and Assumption 3 to show that $\dot{V}_{pv}(t), \dot{I}_L(t) \in \mathcal{L}_\infty$. Above boundedness statements can be used along with Remark 4.1, and the time derivative of (4.5) to show that $\dot{e}(t) \in \mathcal{L}_\infty$. The time derivative of (4.9) can be used along with the above boundedness statements, Remark 4.1 and Assumption 5 to show that $\dot{I}_D(t) \in \mathcal{L}_\infty$. After taking the time derivative

of (4.6), it can be concluded that $\dot{z}(t) \in \mathcal{L}_\infty$. After employing a corollary to Barbalat's lemma [3], it is easy to show that $e(t), z(t) \rightarrow 0$ as $t \rightarrow \infty$.

Generating the Desired Array Voltage Online

In Remark 4.1, it is assumed the desired array voltage, $V_d(t)$, can be designed such that $V_d(t), \dot{V}_d(t)$ and $\ddot{V}_d(t)$ are bounded and $V_d(t) \rightarrow V^*(t)$, where $V^*(t)$ is the unknown optimal array voltage that maximizes the solar power extracted, $P_{pv}(t)$. The extremum-seeking algorithm used in this paper is the incremental conductance MPP tracking algorithm [4]. Unlike many other MPT algorithms, there is no significant loss of efficiency in cases with rapidly changing atmospheric conditions. This algorithm utilizes zero slope regulation to track the maximum power point by comparing the incremental and instantaneous conductances of the PV array and varying the desired voltage, $V_d(t)$ accordingly. Additionally, the algorithm accounts for changes in the atmospheric conditions when the array is operating at maximum power by checking if incremental current is nonzero.

To ensure that $V_d(t), \dot{V}_d(t)$ and $\ddot{V}_d(t)$ are bounded, a filter-based form of the incremental conductance algorithm is used, wherein at each iteration, the discrete guess, $V_d[n]$, is passed through a set of third order stable and proper low pass filters to generate continuous bounded signals for $V_d(t), \dot{V}_d(t)$ and $\ddot{V}_d(t)$. The following filters were used in this study

$$V_d(t) = \frac{\zeta_3}{s^3 + \zeta_1 s^2 + \zeta_2 s + \zeta_3} V_d[n] \quad (4.19)$$

$$\dot{V}_d(t) = \frac{\zeta_3 s}{s^3 + \zeta_1 s^2 + \zeta_2 s + \zeta_3} V_d[n] \quad (4.20)$$

$$\ddot{V}_d(t) = \frac{\zeta_3 s^2}{s^3 + \zeta_1 s^2 + \zeta_2 s + \zeta_3} V_d[n] \quad (4.21)$$

where $s \in \mathbb{C}$ is the Laplace variable, $\zeta_1, \zeta_2, \zeta_3 \in \mathbb{R}^+$ are filter constants and $n \in \mathbb{Z}^+$. The algorithm waits until certain error thresholds are met before making the next guess (i.e., if $|V_d(t) - V_d[n]| \leq e_1$ and $|V_{pv}(t) - V_d(t)| \leq e_2$ then $n = n + 1$; where $e_1, e_2 \in \mathbb{R}^+$ are threshold constants).

Simulation Results

A numerical case study is presented in this section to demonstrate the performance of the control strategy proposed in this paper using MATLAB/Simulink. In this simulation, the obtained average closed loop duty ratio $D(t)$, where $D(t) \triangleq 1 - D'(t)$, is calculated using the actual sampled state variables instead of their averaged values and then used to construct $u(t)$ in (4.1) by modulating the width of a 2 kHz pulse train. The state variables are sampled at 100 kHz.

The simulation plant and control parameters used in the simulation are listed below in Table 4.1.

Parameters	Value	Unit
A	1.6	
C	470	μF
E_{go}	1.1	V
I_{or}	2.0793×10^{-6}	A
I_{sc}	4.8	A
K	1.3805×10^{-23}	Nm/K
k_1	0.01	
k_e	8	
K_I	2.06×10^{-3}	A/°C
k_z	2	
L	4×10^{-3}	H
n_p	1	
n_s	25	
q	1.6×10^{-19}	C
T_r	301.18	K
V_b	24	V

Table 4.1: List of simulation parameters and corresponding values

The atmospheric conditions are assumed to be varying as shown in Fig. 4.2. The tracking error $e(t)$ is shown in Fig. 4.3. From these figures, it can be seen that the tracking error is asymptotically regulated. The synthesized duty ratio function, $D(t)$, is shown in Fig. 4.4 to be bounded. The results of the filter-based incremental conductance algorithm are shown in Fig. 4.5 and 4.6. In Fig. 4.5, the desired array voltage $V_d(t)$ is illustrated. It is clear that $V_d(t)$ is sufficiently differentiable. In Fig. 4.6, the time evolution of the actual power obtained and the maximum power obtainable from the PV array are presented. It should be noted that the actual power converges to the

neighborhood of the maximum power. Fig. 4.7 shows the time evolution of the power obtained using a commonly used strategy wherein the incremental conductance algorithm was applied directly to the duty ratio, $D(t)$, in essence ignoring the dc-dc converter dynamics [5]. This approach is compared to the strategy proposed in this paper using an integral square error performance measure (integral of the error between actual and maximum array power) as shown in Fig 4.8. It is clear that the proposed strategy has a better performance. Overall, the simulation results demonstrated that the proposed control strategy effectively tracks the maximum power point of the photovoltaic array in the midst of varying weather conditions and performs better than a maximum power point tracking (MPPT) control strategy where the converter dynamics are ignored.

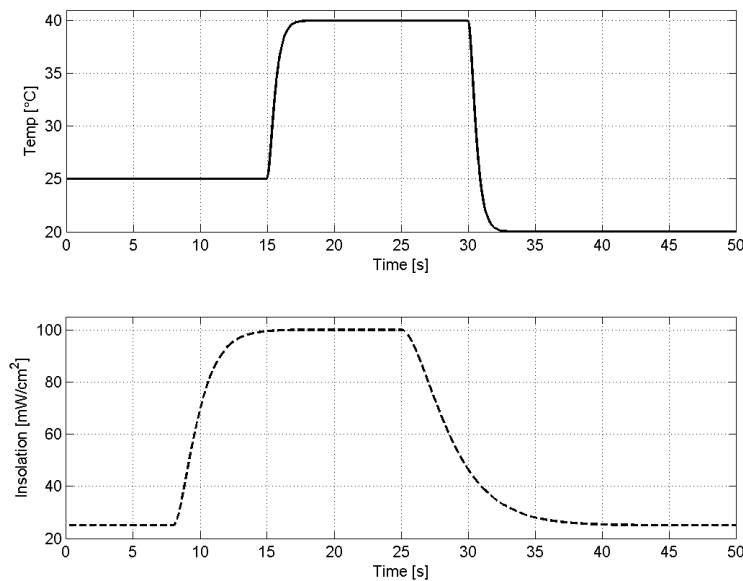


Figure 4.2: Temperature and solar radiation conditions present in the simulation

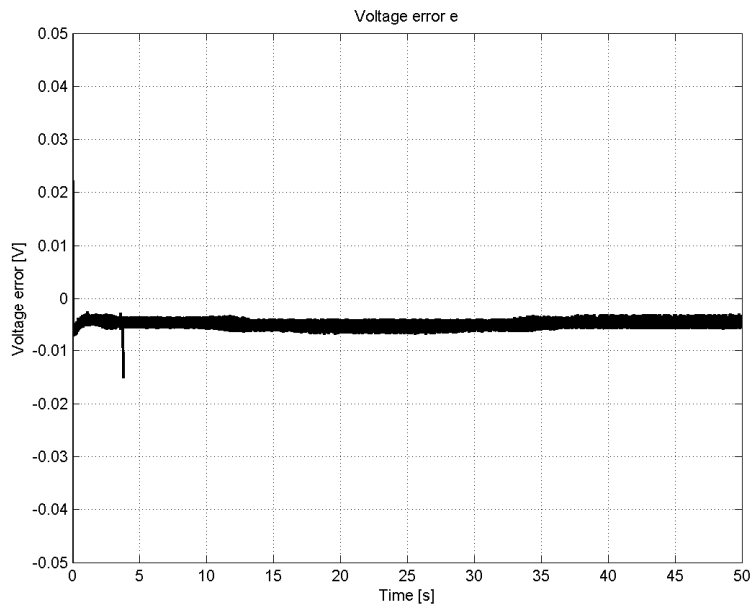


Figure 4.3: Array voltage tracking error $e(t)$

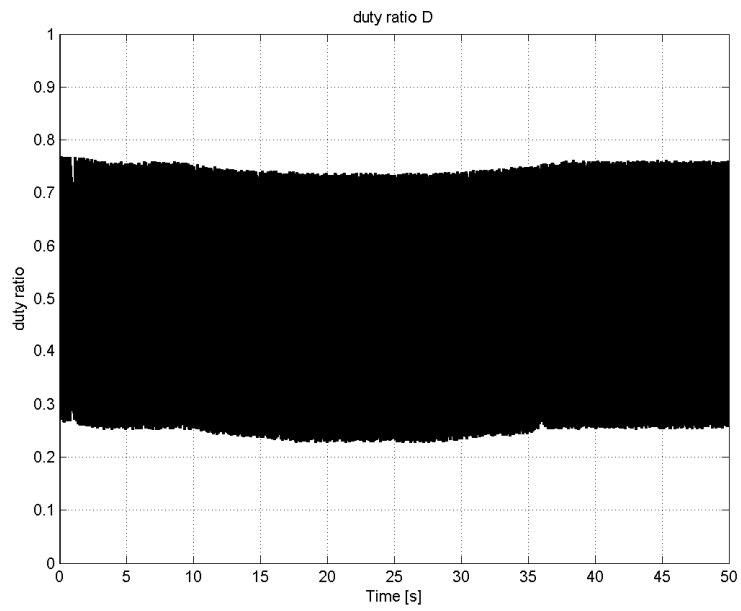


Figure 4.4: Duty ratio $D(t)$

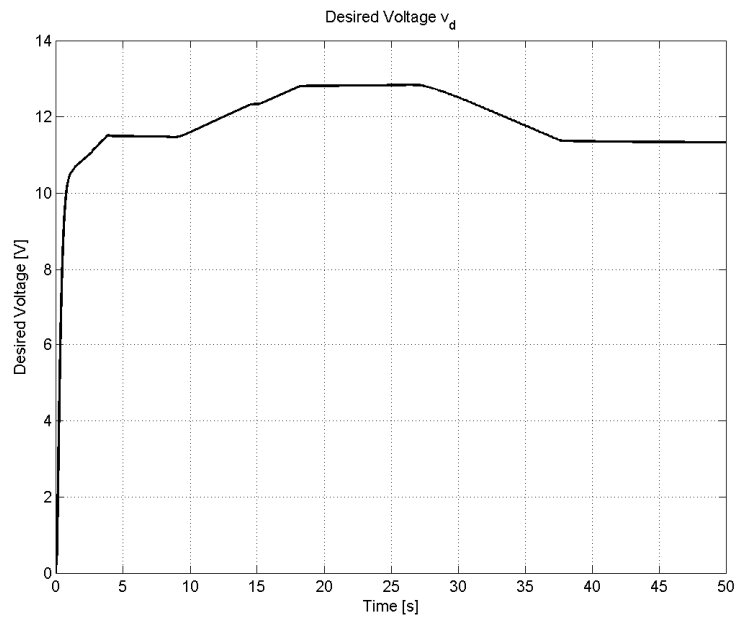


Figure 4.5: Desired array voltage $V_d(t)$

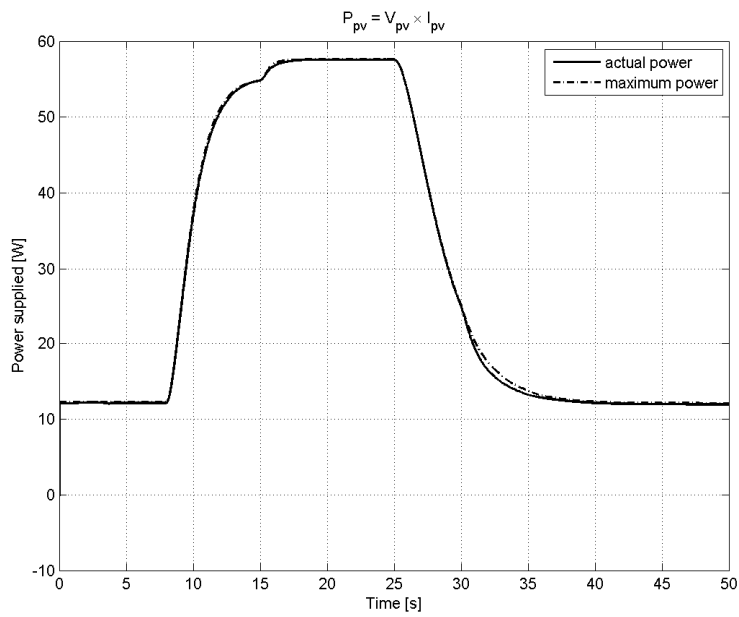


Figure 4.6: Actual and maximum PV array power

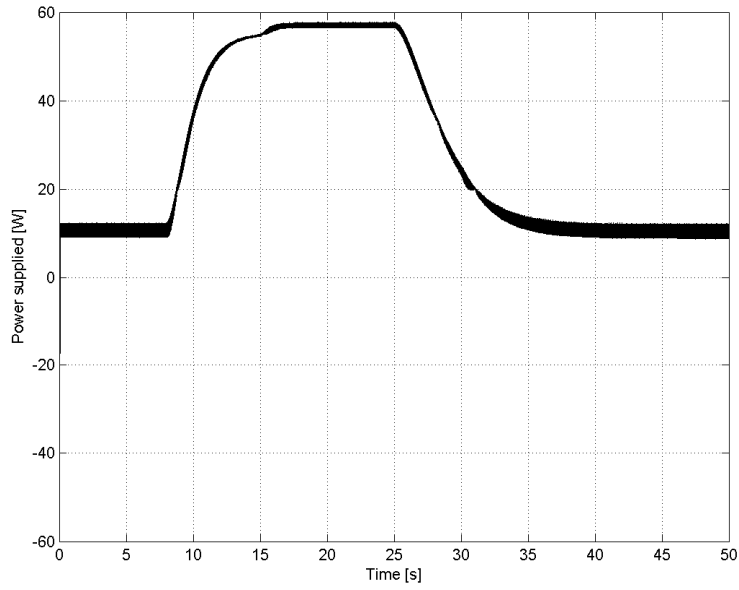


Figure 4.7: Power obtained when converter dynamics are ignored

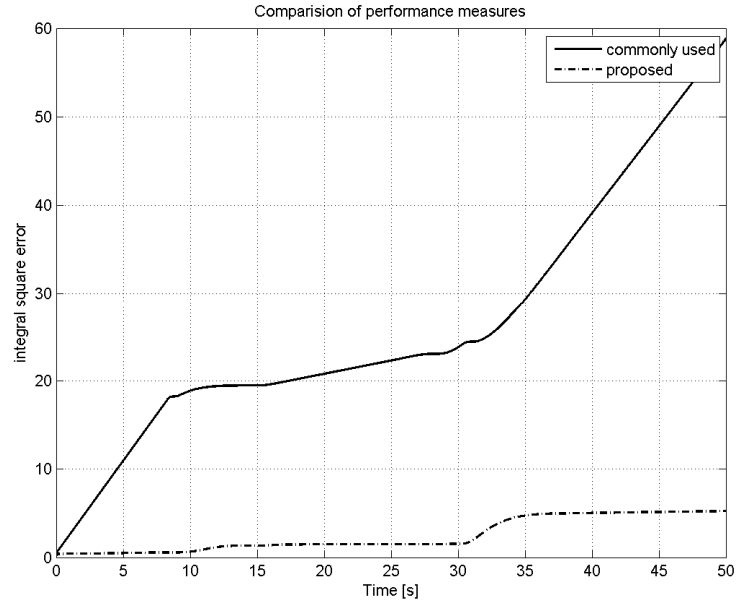


Figure 4.8: Integral square error performance measure

References

- [1] R. Ortega, A. Lorai, P. J. Niklasson and H. Sira-Ramirez, *Passivity-based Control of Euler-Lagrange Systems*, London: Springer-Verlag, 1998, pp. 168-171.
- [2] R. Leyva, C. Alonso, I. Quennec, A. Cid-Pastor, D. Lagrange and L. Martinez-Salamero, "MPPT of photovoltaic systems using extremum-seeking control," *IEEE Trans. Aero Electron. Syst.*, vol. 42, no. 1, pp. 249-258, Jan. 2001.
- [3] J. Slotine and W. Li, *Applied Nonlinear Control*, Englewood Cliffs, NJ: Prentice Hall, 1991.
- [4] K. H. Hussien, I. Muta, T. Hoshino and M. Osakada, "Maximum photovoltaic power tracking: an algorithm for rapidly changing atmospheric conditions," *Proc. IEE-Gener., Transm., Distrib.*, vol. 142, no. 1, pp. 59-64, Jan. 1995.
- [5] Y. Kuo, T. Liang and J. Chen, "Novel maximum-power-point-tracking controller for photovoltaic energy conversion system," *IEEE Trans. Ind. Electron*, vol. 48, no. 3, pp. 594-601, Jun. 2001.

CHAPTER FIVE

CONCLUSIONS

The capability of power harnessing devices for naturally replenishing energy sources must be improved upon in order to increase the viability of renewable energy technologies as an alternative to conventional means of power supply. This dissertation has focused on developing Lyapunov stability-based robust control strategies to maximize the power capture capability of two of the most popular means of renewable technologies, wind and solar power.

In the second chapter, a nonlinear controller has been developed for a variable speed, variable pitch wind turbine system to optimize the power capture efficiency (i.e. *the ratio of power captured to power available*) of the wind turbine at a certain wind speed. The power capture efficiency is a unimodal function of the rotor speed, blade pitch angle and wind speed, and is assumed unknown. A desired blade pitch angle and rotor speed trajectory generator is designed that seeks the unknown set-point that optimizes the power capture while ensuring the trajectory remains bounded and sufficiently differentiable. To track the desired trajectory, a robust controller is developed, which is proven to yield a globally uniformly ultimately bounded stable closed-loop system via Lyapunov-based analysis. The simulation results demonstrated the excellent performance of the robust controller and the numerical-based optimum seeking algorithm.

In the third chapter, a nonlinear control strategy has been developed for a variable speed wind turbine system to the power capture efficiency (i.e. *the ratio of power captured to power available*) of the wind turbine for a particular blade pitch angle and

wind speed. The power capture efficiency is a function of the rotor speed, and wind speed, and is assumed unimodal but unknown. A desired rotor speed trajectory generator is designed to seek the unknown rotor speed that optimizes the power capture, while ensuring the trajectory remains bounded and sufficiently differentiable. To track the desired trajectory, a robust tracking controller is developed to control the rotor speed via the generator rotor voltage. The proposed controller is proven to yield a globally uniformly ultimately bounded result while keeping the closed-loop system stable via Lyapunov-based analysis. Simulation results were provided to verify the effectiveness of the control strategy using a 350W EXTRACTOR wind turbine as a model. Future research will involve the implementation of the control strategy on the EXTRACTOR wind turbine and eliminating the assumption of constant or slowly time varying wind speed.

Finally in chapter four, a backstepping PWM control strategy has been developed to maximize the power extracted from solar generating system, charging a battery via a DC-DC converter, in varying weather conditions. A desired array voltage is designed online using an extremum-seeking algorithm to seek the unknown array voltage that maximizes the output power of the photovoltaic array while remaining bounded and sufficiently differentiable. To track the designed trajectory, a tracking controller is developed to modulate the duty cycle of the boost converter. The proposed controller is proven to yield global asymptotic stability with respect to the tracking errors via Lyapunov analysis. Simulation results are provided to verify the effectiveness of this approach. Finally, the proposed control strategy is compared to a typical maximum power

point tracking algorithm that ignores the dynamics of the boost converter. The performance measure used is the integral square error between the actual and maximum array power. It is shown to perform that the proposed control strategy performed significantly better.

APPENDICES

Appendix A

Proof of Lemma 2.1

The proof for Lemma 2.1 used in Chapter 2 will now be presented. The expression in (2.23) can be substituted into (2.26) and then integrated in time to obtain

$$\int_{t_0}^t L(\tau) d\tau = \int_{t_0}^t \Delta \dot{\tilde{X}}(\tau)^T \left(\dot{f}(\tau) - \rho_0 \operatorname{sgn}(\dot{\tilde{X}}(\tau)) \right) d\tau + \left[\int_{t_0}^t \frac{d\dot{\tilde{X}}^T}{d\tau} \dot{f}(\tau) d\tau \right] - \rho_0 \int_{t_0}^t \ddot{\tilde{X}}^T(\tau) \operatorname{sgn}(\dot{\tilde{X}}(\tau)) d\tau. \quad (\text{A.1})$$

The bracketed term in (A.1) may be integrated by parts so that the simplified expression becomes

$$\int_{t_0}^t L(\tau) d\tau = \int_{t_0}^t \Delta \dot{\tilde{X}}(\tau)^T \left(\dot{f}(\tau) - \frac{\ddot{f}(\tau)}{\Delta} - \rho_0 \operatorname{sgn}(\dot{\tilde{X}}(\tau)) \right) d\tau + \dot{\tilde{X}}(t) \dot{f}(t) - \dot{\tilde{X}}(t_0) \dot{f}(t_0) - \rho_0 \|\dot{\tilde{X}}(t)\|_1 + \rho_0 \|\dot{\tilde{X}}(t_0)\|_1. \quad (\text{A.2})$$

An upper bound on the right hand side of (A.2) can be written as

$$\int_{t_0}^t L(\tau) d\tau = \int_{t_0}^t \Delta \|\dot{\tilde{X}}(\tau)\|_1 \left(\|\dot{f}(\tau)\| + \frac{\|\ddot{f}(\tau)\|}{\Delta} - \rho_0 \right) d\tau + \|\dot{\tilde{X}}(t)\|_1 (\|f(t)\| - \rho_0) + \rho_0 \|\dot{\tilde{X}}(t_0)\|_1 - \dot{\tilde{X}}(t_0)^T f(t_0). \quad (\text{A.3})$$

From (A.3), if $\rho_0 > \|\dot{f}(\cdot)\| + \frac{\|\ddot{f}(\cdot)\|}{\Delta}$, then Lemma 2.1 holds.

Appendix B

Simulation Parameters for Chapter 2

Table B.1 shows the values of the parameters used in the numerical simulation of Chapter 2.

Variables	Value	Units
M	$\begin{bmatrix} 5 & 0 \\ 0 & 5 \end{bmatrix}$	kg.m ²
R	2	m
ν	1.5	m.s ²
A	12.6	m ²
ρ	1.2	kg/m ³
ε	0.1	-
K	10	-
μ	3	-
k	10	-
Δ	2	-

Table B.1: Simulation parameters and values

Appendix C

Generating the Stator Flux Online

$\Psi_{s_1}^d(t)$ is designed to be a strictly positive function that ensures $\Psi_{s_1}^d(t), \dot{\Psi}_{s_1}^d(t), \ddot{\Psi}_{s_1}^d(t)$ are bounded and an optimum reduction in copper loss. The copper loss denoted by $P_{loss}(t)$, is defined as

$$\begin{aligned} P_{loss} &= Power_{in} - Power_{out} \\ P_{loss} &= I_r^T V_r + \tau \omega - I_s^T I_s R_L \end{aligned} \quad (C.1)$$

Substituting (3.16), (3.17), (3.19) and (3.20) into (C.1) results in

$$\begin{aligned} P_{loss} &= (\kappa_1 \Psi_r - \kappa_2 \Psi_s)^T (\dot{\Psi}_r + R_r \kappa_1 \Psi_r - R_r \kappa_2 \Psi_s + J \Psi_r \omega_s - n_p \omega J \Psi_r) + \tau \omega \\ &\quad - R_L (\kappa_1 \Psi_s - \kappa_2 \Psi_r)^T (\kappa_1 \Psi_s - \kappa_2 \Psi_r). \end{aligned} \quad (C.2)$$

At steady state, the system is tracking where all time derivatives equal zero and

$\Psi_r \rightarrow \Psi_r^d, \Psi_s \rightarrow \Psi_s^d, \tau \rightarrow \tau_d, \omega \rightarrow \omega_d$ results in the following

$$\begin{aligned} P_{loss} &= (\kappa_1 \Psi_r^d - \kappa_2 \Psi_s^d)^T (R_r \kappa_1 \Psi_r^d - R_r \kappa_2 \Psi_s^d - n_p \omega_d J \Psi_r^d) + \tau_d \omega_d \\ &\quad - R_L (\kappa_1 \Psi_s^d - \kappa_2 \Psi_r^d)^T (\kappa_1 \Psi_s^d - \kappa_2 \Psi_r^d) \end{aligned} \quad (C.3)$$

$$\tau_d = -\hat{f}_s \quad \Psi_{r_2}^d = \frac{\hat{f}_s}{\alpha \Psi_{s_1}^d} \quad (C.4)$$

$$\Psi_{r_1}^d = \frac{\kappa_1}{\kappa_2} \Psi_{s_1}^d \quad \omega_s = \frac{R_o \kappa_2 \hat{f}_s}{\alpha \Psi_{s_1}^{d^2}} \quad (C.5)$$

After substituting (C.4) and (C.5) into (C.3), P_{loss} can be expressed as a function of $\Psi_{s_1}^d$ as

$$\begin{aligned}
P_{loss} = & \left[\frac{\kappa_1^4 R_r}{\kappa_2^2} + \kappa_2^2 R_r - 2\kappa_1^2 R_r \right] (\Psi_{s_1}^d)^2 \\
& + \left[\frac{\kappa_1^2 R_r \hat{f}_s^2}{\alpha^2} + \frac{\kappa_2^2 R_o \hat{f}_s^2}{\alpha^2} - \frac{R_L \kappa_2^2 \hat{f}_s^2}{\alpha^2} \right] \frac{1}{(\Psi_{s_1}^d)^2} - \frac{\kappa_2 n_p \omega_d \hat{f}_s}{\alpha} - \hat{f}_s \omega_d
\end{aligned} \tag{C.6}$$

The expression in (C.6) is then used as cost function in a filter-based SQE numerical minimization algorithm, similar to the strategy described in optimization section of Chapter 3, with $\Psi_{s_1}^d(t)$ as the functional value. This ensures an optimum reduction in copper losses and that $\Psi_{s_1}^d(t), \dot{\Psi}_{s_1}^d(t), \ddot{\Psi}_{s_1}^d(t) \in \mathcal{L}_\infty$.

Appendix D

Auxiliary Signal Definitions

The terms Ω_i and Θ_j where $i=1, \dots, 13$ and $j=1, \dots, 13$, introduced in (3.34)

and (3.35), are given by

$$\begin{aligned}
 \Theta_1 &= \frac{\kappa_1}{\kappa_2} - \frac{(R_o \kappa_1 - \kappa_{s_1})}{R_o \kappa_2} \\
 \Theta_2 &= \frac{\kappa_1}{\kappa_2} \frac{(R_o \kappa_1 - \kappa_{s_1})}{R_o \kappa_2} + R_r \kappa_2 \\
 \Theta_3 &= R_o \kappa_1 - \kappa_{s_1} + R_r \kappa_1 \\
 \Theta_4 &= n_p \omega - \omega_s + \frac{\alpha \hat{f}_s}{R_o \kappa_2 M_m} \\
 \Theta_5 &= \left[\frac{\hat{f}_s \dot{\Psi}_{s_1}^d}{R_o \kappa_2 \Psi_{s_1}^{d^2}} + \frac{\hat{f}_s}{R_o \kappa_2} \left[\frac{K}{M_m \Psi_{s_1}^d} - \frac{2\rho}{M_m \varepsilon \Psi_{s_1}^d} \frac{\partial \rho}{\partial \omega} e \right. \right. \\
 &\quad \left. \left. + \frac{\rho^2}{M_m \varepsilon \Psi_{s_1}^d} \right] - \frac{\hat{f}_s}{R_o \kappa_2 \Psi_{s_1}^d} + \frac{M_m \ddot{\omega}_d}{R_o \kappa_2 \Psi_{s_1}^d} - \frac{M_m \dot{\omega}_d \dot{\Psi}_{s_1}^d}{R_o \kappa_2 \Psi_{s_1}^{d^2}} \right. \\
 &\quad \left. + \frac{\alpha \Psi_{s_1}^d}{R_o \kappa_2 M_m} \left[K + \frac{\rho^2}{\varepsilon} \right] \right] \\
 \Theta_6 &= \frac{\left[\frac{K \dot{\Psi}_{s_1}^d}{\Psi_{s_1}^{d^2}} + \frac{K^2 \varepsilon + 2K \rho^2}{M_m \varepsilon \Psi_{s_1}^d} - \frac{2\rho}{\varepsilon \Psi_{s_1}^d} \frac{\partial \rho}{\partial \omega} \dot{\omega}_d + \frac{\rho^4}{\varepsilon \Psi_{s_1}^{d^2}} \right]}{R_o \kappa_2}
 \end{aligned}$$

$$\Theta_7 = \frac{1}{R_o \kappa_2} \left[\frac{2K\rho \frac{\partial \rho}{\partial \omega}}{M_m \varepsilon \Psi_{s_1}^d} + \frac{2\rho^3 \frac{\partial \rho}{\partial \omega}}{M_m \varepsilon^2 \Psi_{s_1}^d} \right]$$

$$\Theta_8 = \left[R_o \kappa_2 + \frac{(\alpha \Psi_{r_2}^d)^2}{R_o \kappa_2 M_m} + \frac{\kappa_1}{\kappa_2} (R_o \kappa_1 - \kappa_{s_1}) + R_r \kappa_2 \right]$$

$$\Theta_9 = \frac{\alpha}{R_o \kappa_2} \left[\frac{K}{M_m \Psi_{s_1}^d} - \frac{2\rho \frac{\partial \rho}{\partial \omega} e}{M_m \varepsilon \Psi_{s_1}^d} + \frac{\rho^2}{M_m \varepsilon \Psi_{s_1}^d} \right]$$

$$\Theta_{10} = \left[\frac{\alpha^2 \Psi_{r_1}^d \Psi_{r_2}^d}{R_o \kappa_2 M_m} + \frac{(R_o \kappa_1 - \kappa_{s_1}) \omega_s}{R_o \kappa_2} \right]$$

$$\Theta_{11} = \left[\alpha - \frac{\alpha \Psi_{r_1}^d}{R_o \kappa_2} \left[\frac{K}{M_m \Psi_{s_1}^d} - \frac{2\rho \frac{\partial \rho}{\partial \omega} e}{M_m \varepsilon \Psi_{s_1}^d} + \frac{\rho^2}{M_m \varepsilon \Psi_{s_1}^d} \right] \right]$$

$$\Theta_{12} = \frac{\alpha^2 \Psi_{r_2}^d}{R_o \kappa_2 M_m}$$

$$\Theta_{13} = \left[-(R_o \kappa_1 - \kappa_{s_1}) - R_r \kappa_1 + \kappa_{r_1} + \frac{\rho_1^2}{\varepsilon_1} \right]$$

$$\begin{aligned}
\Omega_1 &= \frac{\dot{f}_s}{\alpha \Psi_{s_1}^d} \left[\frac{M_m \ddot{\omega}_d}{\alpha \Psi_{s_1}^d} - \frac{M_m \dot{\omega}_d \dot{\Psi}_{s_1}^d}{\alpha \Psi_{s_1}^{d^2}} - R_r \kappa_1 \Psi_{r_2}^d \right. \\
&\quad \left. + n_p \omega \Psi_{r_1}^d - \Psi_{r_1}^d \omega_s \right] \\
\Omega_2 &= \left[\frac{K}{\alpha M_m \Psi_{s_1}^d} - \frac{2\rho \frac{\partial \rho}{\partial \omega} e}{\alpha M_m \varepsilon \Psi_{s_1}^d} + \frac{\rho^2}{\alpha M_m \varepsilon \Psi_{s_1}^d} + \frac{\dot{\Psi}_{s_1}^d}{\alpha \Psi_{s_1}^{d^2}} \right] \\
\Omega_3 &= \left[\alpha \Psi_{s_1}^d - \frac{K \dot{\Psi}_{s_1}^d}{\alpha \Psi_{s_1}^{d^2}} - \frac{K^2}{\alpha M_m \Psi_{s_1}^d} - \frac{2K\rho^2}{\alpha M_m \varepsilon \Psi_{s_1}^d} \right. \\
&\quad \left. + \frac{2\rho \frac{\partial \rho}{\partial \omega} \dot{\omega}_d}{\alpha \varepsilon \Psi_{s_1}^d} - \frac{\rho^4}{\alpha M_m \varepsilon^2 \Psi_{s_1}^d} - \frac{\rho^2 \dot{\Psi}_{s_1}^d}{\alpha \varepsilon \Psi_{s_1}^d} \right] \\
\Omega_4 &= \left[\frac{K}{M_m \Psi_{s_1}^d} - \frac{\left(2\rho \frac{\partial \rho}{\partial \omega} e - \rho^2 \right)}{M_m \varepsilon \Psi_{s_1}^d} \right] \\
\Omega_5 &= \left[R_r \kappa_1 - \frac{K \Psi_{r_1}^d}{M_m \Psi_{s_1}^d} + \frac{\left(2\rho \frac{\partial \rho}{\partial \omega} e - \rho^2 \right) \Psi_{r_1}^d}{M_m \varepsilon \Psi_{s_1}^d} + R_r \kappa_2 \right] \\
\Omega_6 &= \frac{\alpha}{R_o \kappa_2} \left[\frac{K}{M_m} - \frac{\left(2\rho \frac{\partial \rho}{\partial \omega} e - \rho^2 \right)}{M_m \varepsilon} \right] \\
\Omega_7 &= \frac{\Omega_6}{\Psi_{s_1}^d} \\
\Omega_8 &= \frac{R_o \kappa_2}{\alpha} \Omega_6 \\
\Omega_9 &= \left[\frac{K}{M_m} - \frac{\left(2\rho \frac{\partial \rho}{\partial \omega} e - \rho^2 \right)}{M_m \varepsilon} - R_r \kappa_1 + \kappa_{r_1} + \frac{\rho_2^2}{\varepsilon_2} \right] \\
\Omega_{10} &= \left[\frac{2K\rho \frac{\partial \rho}{\partial \omega}}{\alpha M_m \varepsilon \Psi_{s_1}^d} + \frac{2\rho^3 \frac{\partial \rho}{\partial \omega}}{\alpha M_m \varepsilon^2 \Psi_{s_1}^d} \right]
\end{aligned}$$

where $\kappa_{r_1}, \kappa_{r_2} \in \mathbb{R}^+$ are control gains, $\varepsilon_1, \varepsilon_2 \in \mathbb{R}^+$ are small constants and

$\rho_1(\cdot), \rho_2(\cdot) \in \mathbb{R}^+$ are known functions designed in Appendix E.

Appendix E

Design of Bounding Terms

The functions $\rho(\bullet)$, $\rho_1(\bullet)$ and $\rho_2(\bullet)$ are designed to ensure that the conditions in Remarks 3.2 and 3.7 are met

$$\rho(\bullet) = \left| \frac{1}{2} \rho_a A \frac{0.45}{\omega} v^3 \right| \quad (\text{E.1})$$

$$\rho_1(\bullet) = \left| \frac{\rho(\bullet)}{R_s \kappa_2 M_m \Psi_{s_1}^d} \left[\frac{2\rho|\partial\rho|e^2}{\varepsilon} + \frac{2\rho^2|e|}{\varepsilon} \right] \right| \quad (\text{E.2})$$
$$+ 2K|e| + M_m|\dot{\omega}_d| + |\hat{f}_s|$$

$$\rho_2 = \left| \frac{\rho(\bullet)}{\alpha M_m \Psi_{s_1}^d} \left(K + \frac{\rho(\bullet) + 2\rho|\partial\rho e|}{\varepsilon} \right) \right| \quad (\text{E.3})$$

Appendix F

Proof of Lemma 3.1

The equation (3.50) can be substituted into (3.53) and then integrated in time to obtain

$$\int_{t_0}^t L(v) dv = \int_{t_0}^t k \tilde{\omega}(v) \left(\dot{f}(v) - \rho_0 \operatorname{sgn}(\tilde{\omega}(v)) \right) dv + \left[\int_{t_0}^t \dot{\tilde{\omega}}(v) \dot{f}(v) d\tau \right] - \rho_0 \int_{t_0}^t \dot{\tilde{\omega}}(v) \operatorname{sgn}(\tilde{\omega}(v)) d\tau. \quad (\text{F.1})$$

The bracketed term in (F.1) may be integrated by parts to obtain the following expression

$$\int_{t_0}^t L(v) dv = \int_{t_0}^t k \tilde{\omega}(v) \left(\dot{f}(v) - \frac{\ddot{f}(v)}{k} - \rho_0 \operatorname{sgn}(\tilde{\omega}(v)) \right) dv + \tilde{\omega}(t) \dot{f}(t) - \tilde{\omega}(t_0) \dot{f}(t_0) - \rho_0 \left| \tilde{\omega}(t) \right| + \rho_0 \left| \tilde{\omega}(t_0) \right|. \quad (\text{F.2})$$

An upper bound on the right hand side of (F.2) can be written as

$$\int_{t_0}^t L(v) dv \leq \int_{t_0}^t k \left| \tilde{\omega}(v) \right| \left(\left| \dot{f}(v) \right| + \frac{\left| \ddot{f}(v) \right|}{k} - \rho_0 \right) dv + \rho_0 \left| \tilde{\omega}(t_0) \right| - \tilde{\omega}(t_0) \dot{f}(t_0) + \left| \tilde{\omega}(t) \right| \left(\left| \dot{f}(t) \right| - \rho_0 \right) \quad (\text{F.3})$$

From (F.3), it is clear that if $\rho_0 > \left| \dot{f}(\cdot) \right| + \frac{\left| \ddot{f}(\cdot) \right|}{k}$, then Lemma 3.1 holds.

Appendix G

Simulation Parameters for Chapter 3

Table G.1 lists the parameter values used in the numerical simulation discussed in Chapter 3.

Parameters	Value	Units
K	50	-
k_f	10	-
L_s	0.078	H
M	0.571	H
M_m	2.4	kg.m ²
n_p	1	-
R_a	1.52	m
R_L	1	Ω
R_r	7.25	Ω
R_s	5.55	Ω
v	2.3	m/s ²
β	2.4	deg
Δ	10	-
ε	100	-
ε_1	1	-
ε_2	1	-
κ_{r_1}	1	-
κ_{r_2}	1	-
κ_{s_1}	50	-
κ_{s_2}	50	-
ρ_a	1.2	kg/m ³
σ	0.25	-

Table G.1: Simulation parameters and values